The Pennsylvania State University

The Graduate School

LOW-TEMPERATURE ELECTRON WIND FORCE ANNEALING THROUGH ELECTROPULSING TREATMENT

A Thesis in

Mechanical Engineering

by

Logan C. Sharp

© 2022 Logan C. Sharp

Submitted in Partial Fulfillment
of the Requirements
for the Degree of

Master of Science

May 2022

The thesis of Logan C. Sharp was reviewed and approved by the following:

Aman Haque
Professor of Mechanical Engineering
Thesis Advisor

Donghai Wang
Professor of Mechanical Engineering

Daniel Haworth
Professor of Mechanical Engineering
Associate Head of Graduate Programs in Mechanical Engineering

ABSTRACT

Electropulsing treatment (EPT) is an effective alternative to traditional heat treatment (HT) for eliciting microstructural and material property changes in metallic materials. EPT can provide benefits of increased energy savings, increased cost savings, and reduced lead times for post-processed materials. Furthermore, certain materials may not be able to undergo HT due to oxidation or other material-specific effects. This study will investigate post-process EPT as an alternative to HT for two specific materials: two-dimensional (2D) layered titanium carbide ($Ti_3C_2T_x$) MXene and nickel-titanium (NiTi) shape memory alloy (SMA). 2D layered carbides and nitrides of transition metals, known as MXenes, have become emergent materials for applications in energy storage, conversion, and transport, due to advantageous electrical, thermal, and mechanical properties. Due to their processing, MXenes must be annealed to reduce their resistivity and reach their theoretical capacitance. However, conventional HT in oxygen-containing environments results in structural oxidation of the most prominent MXene, $Ti_3C_2T_x$, negatively impacting its properties. In this study, a novel, room temperature (RT), electron wind force (EWF) annealing process consisting of EPT and compressive loading is utilized to reduce resistivity by > 90% for $Ti_3C_2T_x$ film. An EWF annealing process consisting of exclusively EPT results in a resistivity reduction of > 75% for $Ti_3C_2T_x$ film. The process of EPT and compressive loading is shown to be mostly permanent, while the process of exclusively EPT is completely permanent. Because both processes can be completed at RT, they can also be performed in ambient conditions. Characterization techniques of Raman spectroscopy and focused ion beam (FIB) scanning electron microscopy (SEM) reveal no changes in composition for $Ti_3C_2T_x$, but a decrease in average internal pore size by transforming a majority of pores to a size of < 600 nm^2. SMAs are a multifunctional class of materials that react to specific stimuli, such as temperature and stress. The most prominent SMAs are NiTi alloys. Beyond typical properties of SMAs, such

as shape memory and strain recovery, NiTi SMAs are known for their corrosion resistance, damping capacity, and biocompatibility, making them ideal for applications in actuation, structures, and medical implants. Although NiTi SMAs are commonly heat treated, EWF annealing through direct current (DC) treatment, EPT, and electropulse rolling (EPR), have shown to be effective in reducing cost and lead time for these alloys. In this study, EPT of 50.7 at.% Ni–49.3 at.% Ti wire is optimized by investigating a wide range of electropulsing parameters, which result in a resistivity reduction of > 8%. Temperatures generally fall below what other studies have reported, with the largest resistivity reductions occurring < 275 °C.

TABLE OF CONTENTS

LIST OF FIGURES

LIST OF TABLES

LIST OF ACRONYMS

2D – two-dimensional

3D – three-dimensional

AM – additive manufacturing

CR – cold rolling

DC – direct current

EPR – electropulse rolling

EPT – electropulsing treatment

EWF – electron wind force

FIB – focused ion beam

FWHM – full width at half maximum

HT – heat treatment

NSF – National Science Foundation

RMS – root mean squared

RT – room temperature

SEM – scanning electron microscopy/microscope

SMA – shape memory alloy

US – United States

UTS – ultimate tensile strength

YS – yield strength

ACKNOWLEDGEMENTS

I would like to first acknowledge my advisor, Dr. Aman Haque, for his continuous support, patience, knowledge, and passion throughout my research and graduate studies. The work in this thesis would not be possible without Dr. Haque's guidance. Second, I would like to acknowledge my lab partners in the Nano-Mechanical Systems Laboratory: Md. Abu Jafar Rasel, Lawrence Bradley, and Nahid Sultan Al-Mamun, for their help with training, idea generation, material characterization, and lab enjoyment. Specifically, I would like to acknowledge Md. Abu Jafar Rasel and Dr. Maxwell Wetherington for help characterizing $Ti_3C_2T_x$ MXene by performing Raman spectroscopy, as well as Nahid Sultan Al-Mamun for help characterizing $Ti_3C_2T_x$ MXene by performing scanning electron microscopy (SEM). Lastly, I would like to thank my family: Jason, Tammy, and Lauren Sharp, as well as my fiancée, Alexis Baublitz (soon to be Sharp), for their continuous love, support, inspiration, and motivation.

This material is based upon work supported by the Division of Civil, Mechanical, & Manufacturing Innovation (Nanomanufacturing program) of the National Science Foundation (NSF) under Award No. 1760931. Any opinions, findings, and conclusions or recommendations expressed in this thesis are those of the author and do not necessarily reflect the views of the NSF.

Chapter 1

Introduction

The first and second sections will detail the methods of traditional heat treatment and the more recent electric current pulsing treatment as processes to elicit microstructural and property changes in various materials. The third and fourth sections will explore $Ti_3C_2T_x$ titanium carbide MXene and nickel-titanium shape memory alloy, respectively, as well as their respective post-processing treatments.

1.1. Traditional Heat Treatment

Traditional heat treatment (HT) is the controlled heating and cooling (typically to extreme temperatures for extended periods of time) of a material to obtain desirable microstructures and material properties. Although certain manufacturing processes, such as casting, welding, forming, and additive manufacturing (AM) or three-dimensional (3D) printing inadvertently lead to thermal changes within a material, HT is often performed as a post-processing strategy to modify the as-manufactured material. On the other hand, HT can also be used as a pre-processing strategy to improve the manufacturability of a material by improving machinability, formability, or restoring ductility. Traditional HT can be divided into thermal processes and thermochemical processes. Thermal HT will be covered in the first subsection, and includes annealing, normalizing, and tempering. On the other hand, thermochemical HT will be covered in the second subsection, and includes hardening and hardening variations [1]. Other varieties of hardening, such as work or strain hardening and precipitation hardening, do not

necessarily require HT, and thus will not be covered. The third subsection will describe some disadvantages of traditional HT.

1.1.1. Thermal Heat Treatment

Thermal HT includes the processes of annealing, normalizing, and tempering. Annealing generally refers to the thermal process of heating a material slowly to the appropriate temperature, holding the material at that temperature for an extended period of time, and cooling the material slowly (usually within the furnace or an insulated material). Annealing is performed to relieve internal or residual stress, decrease hardness, increase ductility, and/or modify the microstructure of the material for end use or further processing [1].

Similar to annealing, normalizing refers to the thermal process of heating a material slowly to the appropriate temperature and holding at that temperature for an extended period of time. However, normalizing differs from annealing in that it is only performed on ferrous metallic materials and that the material cooling is performed in air. Normalizing is performed to provide grain size uniformity and elemental composition within a material. Normalizing generally produces increased hardness and strength, when compared to annealing, for the same material [1].

Tempering refers to the thermal process of heating a material to a temperature lower than its critical point, holding at that temperature for an extended period of time, and cooling the material in still air. Tempering is performed after a hardening process to reduce brittleness of a material and to maintain as much hardness as possible [1].

1.1.2. Hardening and Thermochemical Heat Treatment

As implied by the name, thermochemical HT not only changes the physical properties of a material, but also changes the chemical composition and chemical properties. Thermochemical HT includes the process of hardening and hardening variations. Hardening generally consists of heating a material slowly to the appropriate temperature, holding the material at that temperature for an extended period of time, and cooling the material very quickly (usually by quenching in oil, water, or brine). Hardening processes provide materials with an increase in hardness, but sacrifices ductility, malleability, and formability, leading to an increase in brittleness. As previously mentioned, tempering after hardening can reduce this brittleness while maintaining some hardness [1].

Hardening variations include case hardening, nitriding, carburizing, and cyaniding. Case hardening is a hardening process in which an alloying element (usually C or N) diffuses into the surface of a monolithic metallic material. This results in a material with a hardened surface, while the volume below the surface remains ductile. Nitriding is a specific case hardening process in which N is the alloying element, and the material has previously been heat treated or tempered. Nitriding typically produces the hardest surface of any case hardening process. Carburizing is a specific case hardening process in which C is the alloying element. Lastly, cyaniding is a specific case hardening process in which cyanide is the alloying compound. Cyaniding is a hardening process that is fast and efficient, relative to the other case hardening processes [1].

1.1.3. Disadvantages of Heat Treatment

Although traditional HT is very common, there are some inherent disadvantages to the process. HT is very energy intensive, inefficient, and costly. A 2012 study found that an average

HT facility consumed 9590 MWh of electricity per year [1]. In 2019, the average house in the United States (US) consumed 11000 kWh of electricity per year [2]. The HT facility consumed nearly 900 times more energy than a US household per year. Even with housekeeping measures and energy investments, it was found that the HT facility could only save 12% of energy per year. This high amount of energy consumption leads to increased costs for materials. Additionally, there is typically a long lead time for HT because the furnaces are constantly in use, which is an additional cost for these materials [1]. Furthermore, certain materials may not be able to undergo HT. Although standard materials can undergo HT without consequences (excluding sacrificing hardness for ductility or vice versa), certain specialized materials may undergo structural oxidation or degradation when exposed to elevated temperatures, which can severely hinder properties of a material. HT is not an option for these materials. Because of the disadvantages of HT, other ways of modifying microstructures and properties of a material should be explored.

1.2. Electropulsing Treatment

Since the late 1980s and early 1990s, high current density electric pulses have been applied to a variety of different materials as an alternative to HT, in order to modify microstructures and enhance mechanical properties. The application of these high current density electric pulses, deemed electropulsing treatment (EPT), has resulted in many different outcomes for different materials and different electropulsing parameters [3]. The primary electropulsing parameters responsible for eliciting microstructural changes in materials are current density, pulse width, and pulse frequency [4]. Current density is defined by the amount of electrical current per cross-sectional area of material, measured in units of A/mm^2. Peak current density refers to the amplitude of current density, while root mean squared (RMS) current density can be thought of as the average current density over a period of time. Pulse width is defined as the elapsed time that a

single pulse of current is applied to the material, generally measured in μs. Pulse frequency is defined as the number of current pulses per s of time, measured in Hz. In electropulsing literature, current densities have ranged from tens to thousands of A/mm^2, pulse durations have ranged from 20 to thousands of μs, and pulse frequencies have ranged from 1 to hundreds of Hz [4].

1.2.1. Materials and Applications

Early research on the application of electric current pulses investigated the effects of electroplasticity [5–7] and electromigration [8,9] in metals. Later, and up to the present, EPT has been applied to numerous materials, including copper (Cu) and copper alloys [10–26], titanium (Ti) and titanium alloys [27–42], iron (Fe) alloys [43–46], steels [4,47–82], magnesium (Mg) alloys [83–112], aluminum (Al) alloys [113–125], zinc (Zn) alloys [126–134], tungsten (W) [135] and more, to elicit microstructural changes. Figure 1-1 showcases the microstructures of a copper alloy, titanium alloy, magnesium alloys, and iron steels pre- and post-EPT. The effects of EPT on a material vary depending upon the initial microstructure, crystal orientation, and degree of deformation. Generally, EPT has resulted in microstructural evolution through grain refinement, texture evolution, oriented grains, and redistribution or elimination of pores and inclusions. As defined by the Hall-Petch relationship, small and uniform grains are typically beneficial for mechanical properties. Furthermore, beyond the elimination or pores and inclusions, EPT has been shown to close or heal micro- and macro-voids or cracks in certain materials [50,59,66,77,136,137]. The following subsections describe the changes of strength, plasticity, hardness, and corrosion resistance for these different materials after EPT, as well as the electropulsing parameters that induce the changes. The subsections will also cover crack healing enabled by EPT and mechanisms behind EPT.

Typical metal materials		Untreated by EPT	Treated by EPT	References
Copper alloy	brass	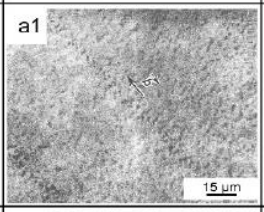	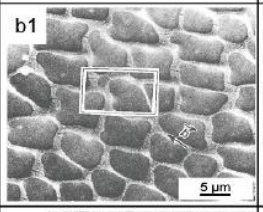	[21]
Titanium alloy	TC4	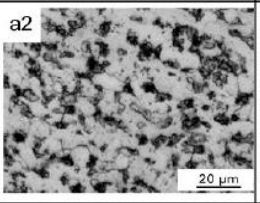	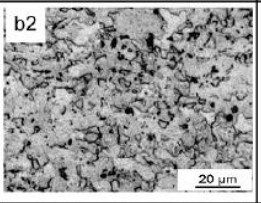	[37]
Magnesium alloy	AZ 31	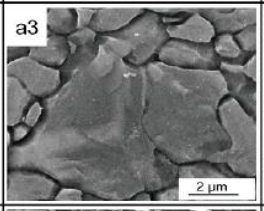	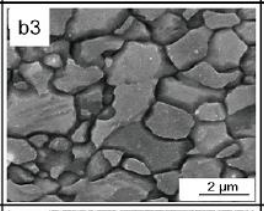	[93]
	AZ 91	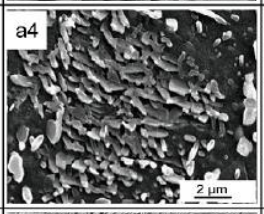	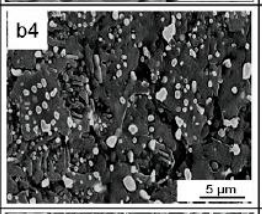	[107]
iron steel	pearlitic steel (0.8% C)	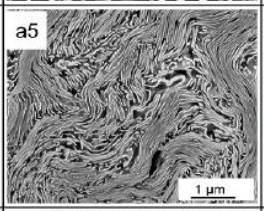	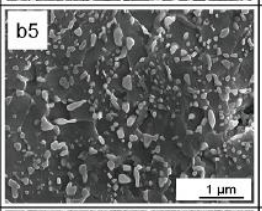	[78]
	TRIP (0.14% C)	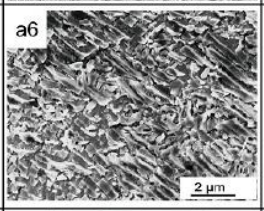	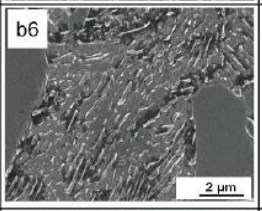	[55]
	316L stainless steel	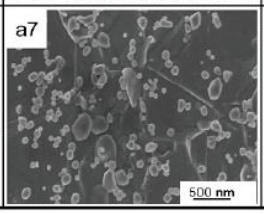	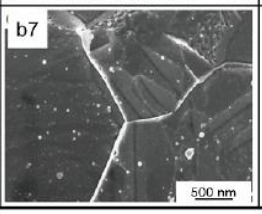	[53]

Figure **1-1**: Microstructures of a copper alloy, a titanium alloy, magnesium alloys, and iron steels, **a1-a7.** before electropulsing treatment, and **b1-b7.** after electropulsing treatment. Reprinted from [3].

1.2.2. Electropulsing Treatment of Copper Alloys

Much of the early research in EPT was performed on pure copper. EPT has resulted in an enhanced recrystallization rate and decreased flow stress for copper and copper alloys. Recrystallization rate refers to the rate at which previous (usually deformed) grains are consumed by the nucleation of new grains that grow to replace the original grains, usually as a result of a heating process. Flow stress refers to the instantaneous amount of stress required to plastically deform a material. EPT of cold worked copper with a peak current density of 800 A/mm^2, pulse frequency of 2 Hz, and pulse duration of 90 μs, has resulted in grain refinement at lower temperatures [11] and grain growth at higher temperatures [10]. The rate of recrystallization was found to improve, while the rate of twinning was found to decline. Twinning refers to adjacent crystal grains that share some of the same crystal lattice points in a symmetrical manner. Furthermore, the treatment of copper with direct current (DC) of an equivalent heating rate did not lead to the reduction same enhancement in recrystallization [19], indicating that there are effects induced by EPT that go beyond Joule heating. Joule heating during EPT refers to impinging electrons being scattered by the crystal lattice of a conducting material (electron lattice interactions) [138]. Impinging electrons will also collide with defects or interfaces within the conducting material (electron-defect interactions), providing a mechanical force or momentum shift from electrons to defects, known as the electron wind force (EWF).

Research on Cu-Zn alloy investigated heating rates between EPT and similar simulated heating rates through a pulsed laser [22]. EPT with a peak current density of 18000 A/mm^2, pulse width of 800 μs, and peak pulse frequency of 8333 Hz, resulted in a heating rate of 1000000 °C/s. A similar heating rate developed through an 1000 μs pulse from an Nd:glass laser. However, β’ phase precipitates were developed after EPT, which were not present after the simulated heating rate from the laser application, indicating that heating and cooling rates alone are not capable of

eliciting microstructural changes in Cu-Zn alloy. For this reason, the changes were attributed to enhanced nucleation rate through a reduction in the thermodynamic barrier, as opposed to high heating and cooling rates. Nucleation rate refers to the rate at which new grains nucleate and begin to grow. The thermodynamic barrier refers to the activation energy necessary to elicit a phase transformation. Furthermore, EPT resulted in the transformation of some α and β' phases to the β phase [25], as well as ultrafine α phase grains [24], which did not occur in the similar simulated heating rate.

1.2.3. Electropulsing Treatment of Titanium Alloys

Titanium and titanium alloys are very common industrial materials due to beneficial properties, such as low density, high strength-to-weight ratio, and high corrosion and erosion resistance [139]. However, titanium is traditionally hard to deform. EPT has been used to increase formability for titanium alloys, as an alternative to hot deforming processes [3]. Through simulation, EPT has shown to be more effective in deforming titanium when combined with traditional deformation processes, like rolling, than with traditional processes alone [139]. This is caused by a decrease in flow stress, which softens titanium and allows for increased elongation [140,141]. The strength of cold rolled TA1-A CP titanium after EPT was found to be significantly higher than annealed samples, while maintaining ductility [39]. This was suggested to be due to the formation of equiaxed grains and lamellar microstructure, leading to a reduction in effective slip distance and an increase in flow stress. The application of a singular electric pulse of 26000 A and pulse width of 400 μs to Ti-6Al-4V induced a martensitic phase transformation from α-Ti to a combination of α-Ti and β-Ti [35]. This phase transformation was attributed to rapid Joule heating. The application of EPT to TC4 titanium alloy sheet resulted in improved plastic deformation with a 48.6% increase in elongation and 19.8% decrease in yield strength (YS) [36].

An even larger improvement in plasticity was achieved in the application of EPT to cold rolled TA15 titanium alloy sheets with a 93% increase in elongation, as shown in Figure 1-2 [38]. This elongation increase was enabled by local recrystallization and damage healing. EPT has also been combined with traditional HT in cold worked α-Ti [27]. This combined treatment resulted in grain refinement when temperatures were maintained below 600 °C and grain growth when temperatures were maintained at 600 °C. Grain refinement was attributed to an enhanced nucleation and recrystallization rate. Table 1-1 summarizes these findings.

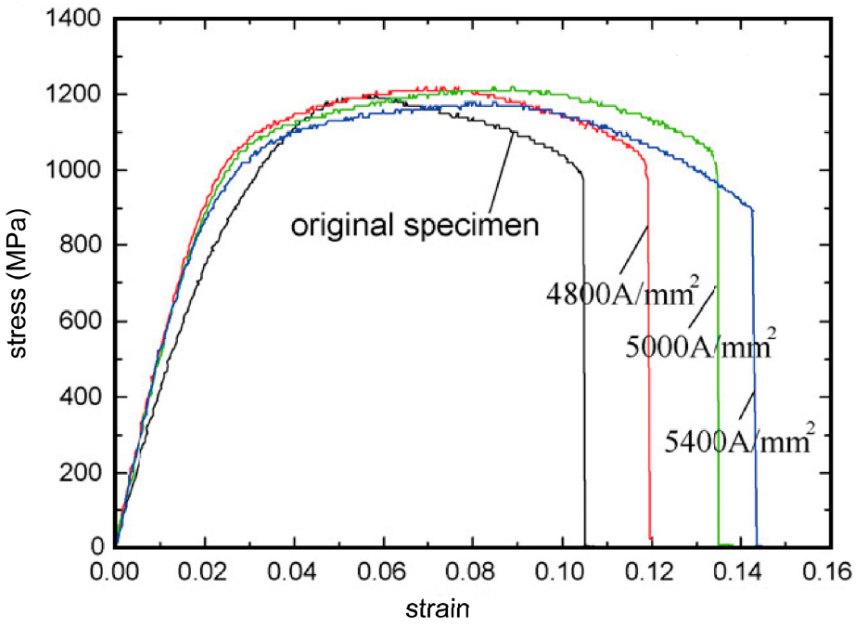

Figure **1-2**: Stress-strain curve of TA15 titanium alloy after electropulsing treatment with varying current densities [38]. Reprinted from [3].

Table **1-1**: Mechanical properties of pure titanium and titanium alloys after electropulsing treatment. Reprinted from [3].

Sample State		Ultimate Tensile Strength (MPa)	Yield Strength (MPa)	Tensile Elongation (%)	Ref.
TA15 sheet	cold-rolled	1175	-	7.2	[38]
	electropulsed	1100	-	13.9	
	increase by (%)	−6	-	+93	
TC4 sheet	annealed	1033	936	15.6	[36]
	electropulsed	947	750	23.18	
	increase by (%)	−8.3	−19.8	+48.6	
TA1-A CP-Ti sheet	annealed	300	210	40	[39]
	electropulsed	400	300	31.5	
	increase by (%)	+33	+43	−21	

EPT has also shown to minimize anisotropy in the deformation of titanium alloys, with current density playing a critical role [3]. TA15 sheets electropulsed with current densities of 4800 and 5000 A/mm^2 display anisotropy, while the anisotropy diminishes with a current density of 5400 A/mm^2 [38]. Similar reductions in anisotropy during plastic deformation have been shown in Ti-6Al-4V [42]. This anisotropy reduction has also been attributed to the conversion of the microstructure to non-directional, equiaxed grains.

1.2.4. Electropulsing Treatment of Iron and Steels

EPT has been performed on numerous iron-based amorphous alloys [43,45,48]. EPT resulted in low temperature recrystallization in both $Fe_{75}B_{15}Si_{10}$ and $Fe_{79}B_{14}Si_7$ alloys [43], and the researchers suggested that the results could not be attributed to Joule heating alone. EPT of $Fe_{78}B_{13}Si_9$ resulted in nanocrystalline grains [45]. The nanograins were attributed to the enhanced nucleation rate enabled by EPT. Similarly, EPT of boron steel with a peak current density of 890 A/mm^2 resulted in a nanocrystalline γ-Fe structure [48]. Again, the nanograins were attributed to the enhanced nucleation rate.

EPT has also resulted in a variety of effects in steels. In low-carbon steel (0.07% C), EPT resulted in a significant increase in UTS, elongation, and microhardness [58]. The fracture mode of the steel also converted from brittle to ductile. These property increases were attributed to the formation of 0.5–3 μm equiaxed ferrite micro and nanograins. Grain sizes were found to decrease with an increase in current density and heating rate. Similarly, additional research investigating EPT of low-carbon steel found that EPT induced a phase transformation to nanosized γ-Fe [69]. This phase transformation was attributed to high heating and cooling rates, while the enhanced nucleation rate of γ-Fe was attributed to a reduction of the thermodynamic barrier.

In medium-carbon steel (0.45% C), EPT with a peak current density of 20000 A/mm^2, pulse width of 160 μs, and frequency of 0.25 Hz, no microstructural changes were found, but the UTS increased from 695 MPa as-quenched to 1180 MPa [60]. The improvement in UTS was attributed to a reduction in dislocation density and residual stress, which was hypothesized to be a result of primarily Joule heating.

In cold rolled silicon steel, EPT resulted in grain refinement from 2–6 μm grains after HT down to 0.5–2 μm grains after EPT [81]. This grain refinement was attributed to an enhanced nucleation rate and retarded recrystallization. In severely-deformed pearlitic steel, the investigation of current magnitude in EPT resulted in a decrease in Vickers hardness for all samples [78], which was attributed to differing degrees of grain refinement, as well as spheroidization of pearlite and cementite particles within the microstructure. Spheroidization refers to the formation of spherical or globular iron carbide forms after heating and (usually slow) cooling. The degree of spheroidization was found to increase with increasing current density. In ferro-pearlitic duplex steel (0.14% C), the relationship between hardness, UTS, YS, and layer spacing were studied after EPT and found to follow the Hall-Petch relationship [55], which confirmed previous results in deformed pearlitic steel [78]. The softening effect in steels after EPT has been attributed to increased lamellar pitch and subsequent spheroidization, allowing

dislocations to move freely within the matrix, as well as the removal of internal voids, creating a zone free of precipitates along the grain boundaries [3,55].

In cold drawn pearlitic steel, a single electropulse with a current density of 9610 A/mm^2 resulted in nanosized spheroidized cementite particles with an average size of 30 nm [80]. Figure 1-3 displays the microstructures before and after EPT. This grain refinement was attributed to the additional free energy provided by EPT.

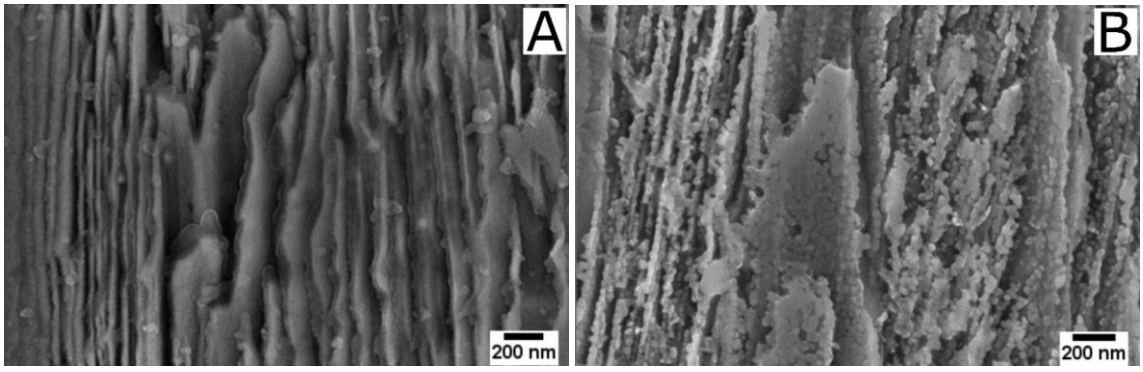

Figure **1-3**: Microstructure of cold drawn pearlitic steel, **a.** before electropulsing treatment, and **b.** after electropulsing treatment. Reprinted from [80].

In DP600 dual phase steel, mechanical properties were significantly improved by EPT-tempering [57]. The UTS, YS, and hardness increased by 38.98%, 8.90%, and 20.90%, respectively. These property increases were attributed to the formation of ultrafine ferrite grains and nanosized cementite particles. EPT was determined to be a suitable alternative method to delay and repair the temper softening problem in dual phase steels. Table 1-2 summarizes the mechanical performances of these steels.

Table **1-2**: Mechanical properties of iron steels after electropulsing treatment. Reprinted from [3].

Sample State		Ultimate Tensile Strength (MPa)	Yield Strength (MPa)	Tensile Elongation (%)	Vickers Hardness (HV)	Ref.
TRIP sheet	hot rolled	700 *	570 *	23 *	230 *	[55]
	electropulsed	630 *	480 *	26 *	180 *	
	increase by (%)	−0	−15.79	+13.04	−21.74	
Low-carbon steel sheet	annealed	580	—	40	179	[58]
	electropulsed	1040	—	45	325	
	increase by (%)	+79	—	+13	+82	
DP600 sheet	cold rolled	1034.25	773.26	3.31	301 ± 8	[57]
	electropulsed	1126.33	1074.66	3.12	364 ± 12	
	increase by (%)	+8.90	+38.98	−5.74	+20.9	

*Mechanical properties are estimated from figures

EPT has shown to be beneficial in providing improvements in fatigue life for certain steels. In electropulsed SUS316 stainless steel, hardness was shown to decrease, while fatigue life was shown to increase [51]. The application of electropulses was shown to delay fatigue crack propagation. The increase in fatigue life of SUS316 stainless steel is displayed through S-N curves in Figure 1-4. A similar increase in fatigue life has been displayed in AISI 304 steel (0.04% C, 1.1% Mn, 0.41% Si, 0.0437% P, 0.0044% S, 18.16% Cr, 8% Ni, 0.0335% Mo, 0.1% V, 0.32% Cu) [62]. The differences in fatigue life for AISI 304 steel are larger for lower stress amplitudes than for larger stress levels.

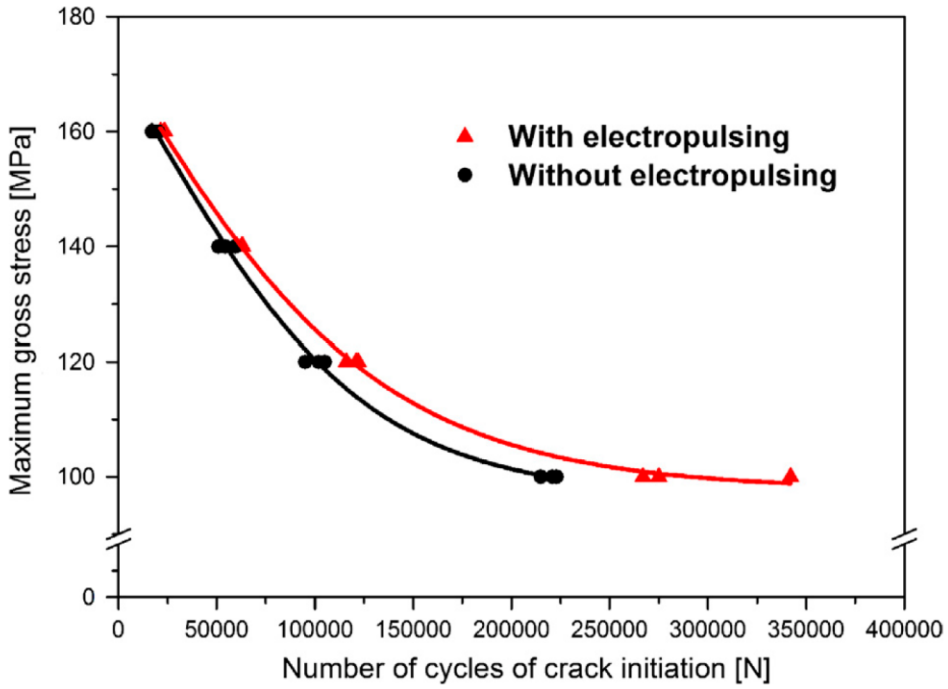

Figure **1-4**: S-N curves of SUS316 stainless steel before and after electropulsing treatment [51]. Reprinted from [3].

Studies have sown EPT to be effective for improving corrosion resistance of steels. EPT of cold brushed steel resulted in elimination of residual stress and a reduction in dislocation density, which reduces the stress corrosion rate [3]. Similarly, EPT of X70 pipeline steel resulted in grain refinement and improved resistance to local corrosion [142]. Enhanced corrosion resistance was also found for 2205 duplex stainless steel due to an increase in the fraction of Σ3 grain boundaries, providing increased resistance to corrosion and decreased electrical resistivity than normal grain boundaries [52].

1.2.5. Electropulsing Treatment of Magnesium Alloys

Magnesium and magnesium alloys have shown promise in biomedical and industrial applications due to advantages, such as high specific strength and low mass density. However,

low absolute strength and poor formability at room temperature have limited their application to an extent. The hexagonal close-packed (HCP) structure of magnesium results in poor plasticity at room temperature, requiring heat treatment for increased formability and improved mechanical properties [3]. EPT has proven to be important for improving both plasticity and strength in magnesium and its alloys by increasing grain boundary slip [90].

EPT has been performed on numerous magnesium alloys. EPT of ZK60 magnesium alloy sheets were found to have increased softness when compared to an equivalent heat treatment for the same length of time [97,100]. This indicates that Joule heating during EPT was not playing the sole role in eliciting microstructural changes. Hardness of the sheets were found to decrease, while the tensile strength and elongation of the sheets were found to increase. Static recrystallization of the grains resulted in finer grain structure and the elimination of work hardening influence.

EPT of AZ31 magnesium alloy also resulted in improved elongation to failure [95]. This elongation could be further improved by optimizing the amounts of the inverse eutectic liquid phases in the inverse eutectic reaction ($\alpha+\beta=L$) induced by EPT [143]. Similarly, EPT resulted in improved ultimate tensile strength (UTS), YS, and elongation to failure for aged, cold rolled AZ91 magnesium alloy strips. The UTS, YS, and elongation to failure increased by 11–12%, 10%, and 70–75%, respectively. Additional research on cold rolled AZ91 found hardness to decrease with increasing pulse frequency, as a result of reduced dislocation density [107,111]. Another study investigated dynamic EPT of AZ91 alloy, where dynamic refers to simultaneous rolling deformation and EPT [89]. Dynamic EPT has also been referred to as electropulsed rolling (EPR). EPT of AZ91 in this study resulted in the decomposition of the β phase with increasing pulse frequency. The phase transformation was accelerated in standard static EPT [87], when compared to dynamic EPT or EPR [89]. The enhanced nucleation rate in AZ31 alloy during EPT has been attributed to both thermal and athermal effects [85]. Table 1-3 displays the results on the

mechanical properties of these alloys after EPT. Figure 1-5 displays how varying pulse width, temperature, pulse frequency, and voltage during EPT affected the mechanical properties of these magnesium alloys.

Table **1-3**: Mechanical properties of magnesium alloys after electropulsing treatment. Reprinted from [3].

Sample State		Hardness (HV)	Ultimate Tensile Strength (MPa)	Yield Strength (MPa)	Tensile Elongation (%)	Refs.
ZK60 sheet	cold rolled	848	210	—	15.7	[96,100]
	Electropulsed	728	320	—	30	
	increase by%	−14.15	+52.4	—	+91	
AZ91 strip	cold rolled	—	330	245	16.2	[92]
	Electropulsed	—	362~370	270	27.6~28.4	
	increase by%	—	+11~12	+10	+70~75	
AZ31 strip	cold rolled	—	315 *	280 *	10	[90,95]
	Electropulsed	—	295~262 *	265~185 *	29~43	
	increase by%	—	−6~18	−5~34 *	+190~330	

*Mechanical properties are estimated from figures

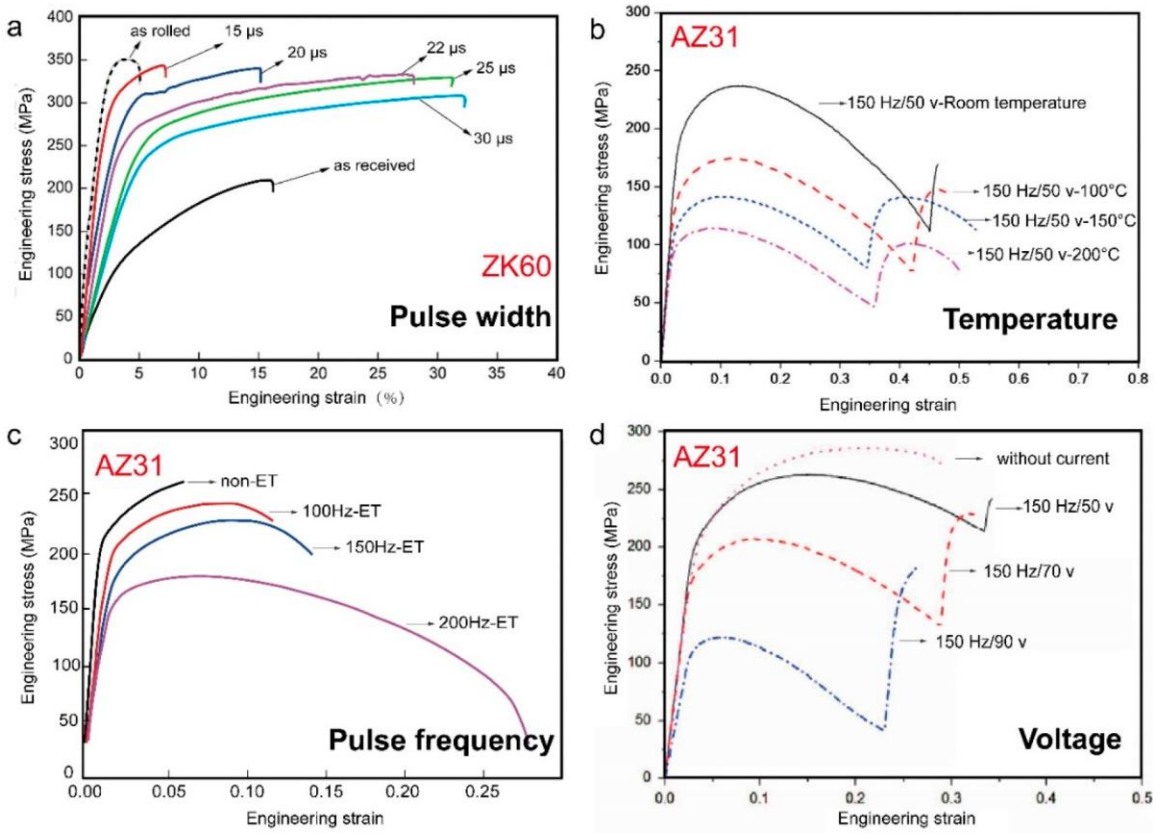

Figure **1-5**: Stress-strain curves of, **a.** ZK60 alloy electropulsed with varying pulse widths [97], **b.** AZ31 alloy electropulsed with varying processing temperatures [98], **c.** AZ31 alloy electropulsed with varying pulse frequencies [84], and **d.** AZ31 alloy electropulsed with varying voltages [83]. Reprinted from [3].

EPT has also resulted in increased corrosion resistance for magnesium alloys. Both EPT and conventional HT of AZ31 magnesium alloy strips have resulted in improved corrosion resistance in 3.5% NaCl solution [144]. This improvement was attributed to recrystallization and a reduction in dislocation density. However, due to the finer grains after EPT, corrosive microcells could form, which would decrease the corrosion resistance over time.

1.2.6. Electropulsing Treatment of Zinc Alloys

Zinc and zinc alloys are beneficial for wear and corrosion resistance, high strength and hardness, and high electrical and thermal conductivity [3]. EPT of zinc alloys has shown to reduce brittleness and improve plasticity. In deformed ZA22 alloy, a maximum 437% increase in elongation has been achieved by EPT with the optimal current of 10 A [126], as shown in Figure 1-6. This drastic increase in elongation was attributed to accelerating the movement of dislocations, as well as homogenizing the distribution of dislocations, resulting in T' phase precipitates and dislocation pinning [129]. Further research on dynamic EPT or EPR of ZA22 alloy with current densities ranging from 35.8–104 A/mm^2 determined that an increase in current density increased decomposition of zinc's η phase [130]. This phase transformation was accelerated in standard static EPT when compared to dynamic EPT or EPR. Table 1-4 summarizes these results.

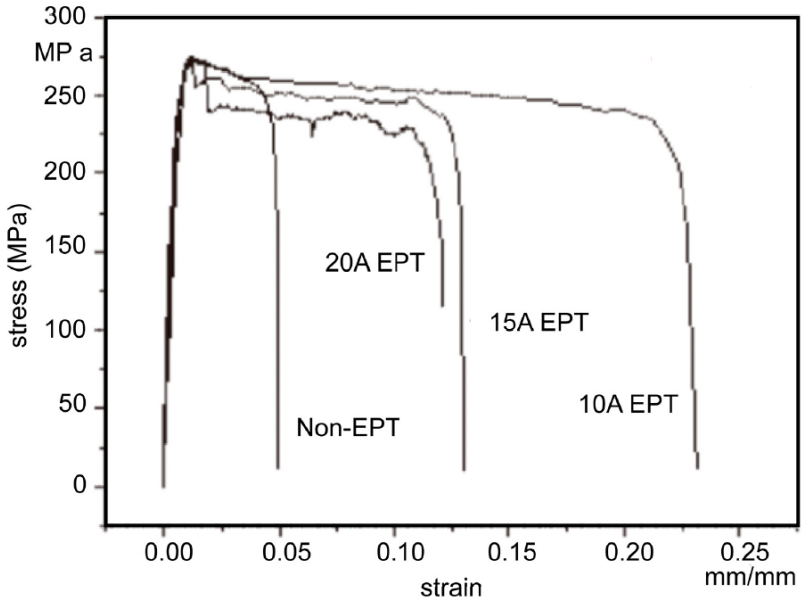

Figure **1-6**: Stress-strain curve of ZA22 alloy after electropulsing treatment with varying currents [126]. Reprinted from [3].

Table **1-4**: Mechanical properties of ZA22 zinc alloy after electropulsing treatment [126]. Reprinted from [3].

Sample State		Peak Current Density (A/mm^2)	Ultimate Tensile Strength (MPa)	Tensile Elongation (%)
ZA22 sheet	non-EPT	-	298	4.5
	EPT	8.13	272	6.4
		12.32	300	8.5
		15.75	260 *	5.5
		21.21	275	6.4

*Mechanical properties are estimated from figures

1.2.7. Crack Healing Induced by Electropulsing Treatment

EPT has been shown to heal cracks or voids in numerous metallic materials, including steels [50,51,59,77,145], titanium alloy [37], and aluminum alloys [113]. Early research in EPT of polycrystalline copper suggested that EPT was capable of reducing intergranular cracking and increasing fatigue life [20]. By researching crack healing of TC4 titanium alloy sheet, it was determined that cracks healed from the crack tip and the width in the center of the cracks decreased [37]. Recrystallization of equiaxed grains at the crack tip slowly bridged the distance of the crack, which indicated that EPT could prevent crack growth. This prevention of crack growth is illustrated in Figure 1-7.

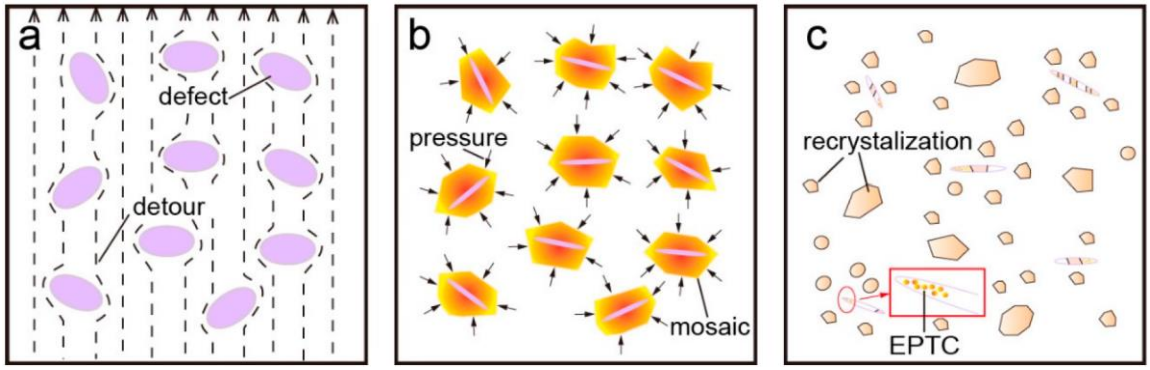

Figure **1-7**: Schematic of crack healing enabled by electropulsing treatment through, **a.** current bypassing defects, **b.** pressure formation around defects, and **c.** recrystallization and electropulsing treatment cladding (EPTC) [37]. Reprinted from [3].

The application of multiple EPTs has led to the complete healing and closure of cracks. After 7 applications of pulsed current, cracks have been completely healed in SUS304 stainless steel [59]. The cracks were healed from the crack tips, resulting in shorter cracks with each subsequent application of EPT, as shown in Figure 1-8. The crack healing was attributed to detour and Joule heating effects. Rapid melting and solidification of the heating areas resulted in columnar grains and a fine recrystallization zone, but inconsistent healing. Three mechanisms were proposed for this crack healing: dislocation movement, atomic diffusion, and thermo-compressive stress.

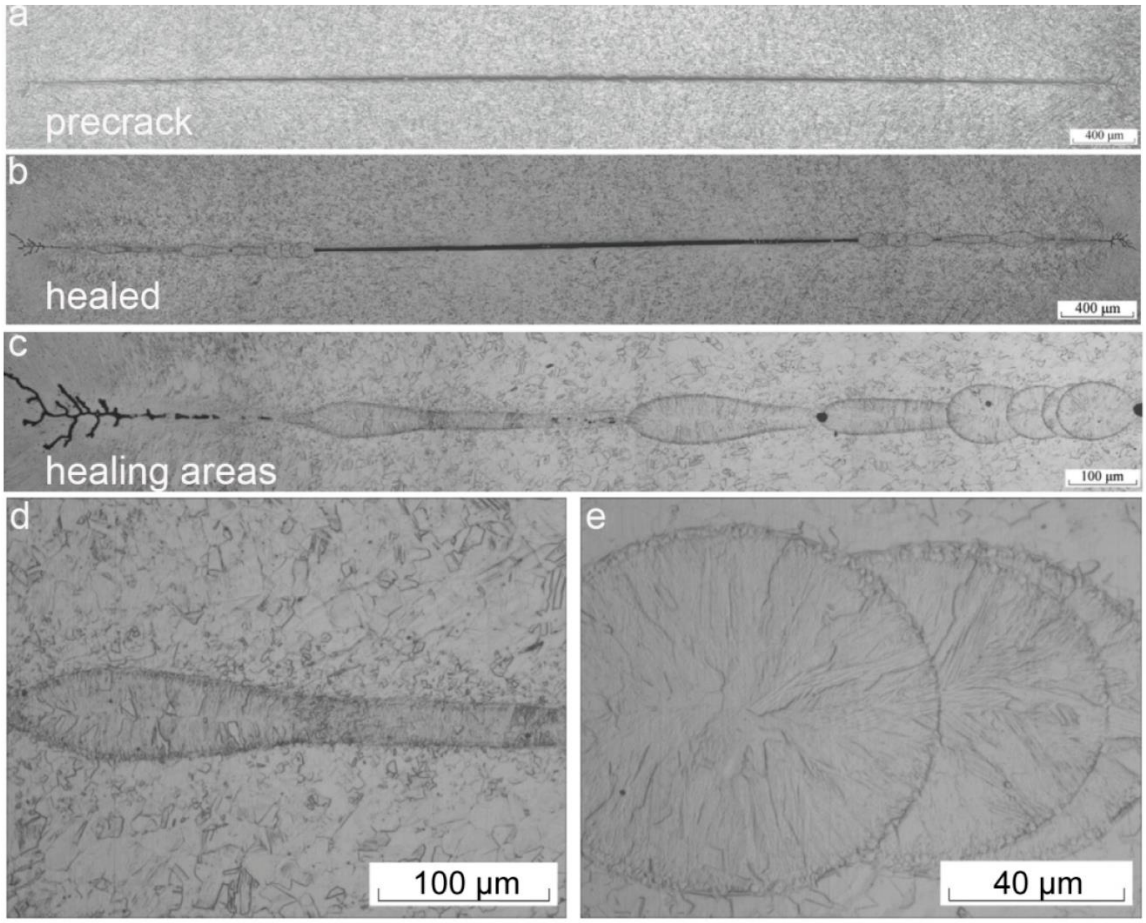

Figure **1-8**: Morphology of, **a.** pre-crack, **b.** healed crack, and **c–e.** enlarged views of healed crack, in SUS304 stainless steel after electropulsing treatment [59]. Reprinted from [3].

Crack healing in medium carbon steel has been theorized to be a result of electrically stressing the steel to produce a low-temperature plasma. However, local thermal expansion around the crack likely influenced atomic movement towards the crack face, resulting in the crack faces merging when thermal expansion was sufficient [77]. The microstructure surrounding the crack remained unchanged. Fatigue cracks have also been healed in austenitic stainless steel through the selective effect [50,145]. Because the electric resistance is higher on the crack surface, thermal compressive stress was generated to heal the crack tip. Repeated applications of EPT resulted in complete crack healing, as shown in Figure 1-9.

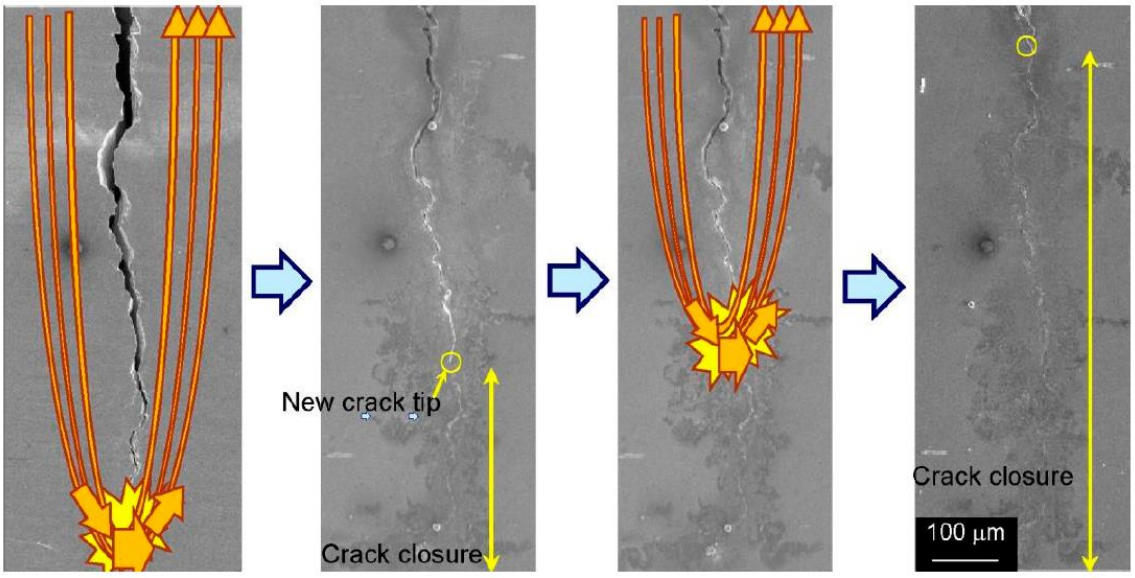

Figure **1-9**: Closure of fatigue crack in austenitic stainless steel after multiple applications of electropulsing treatment [145]. Reprinted from [3].

A thermodynamic model of crack healing through EPT has also been developed [136]. This model incorporates current density, crack geometry, and driving healing force. This research suggests that beyond a critical current density, crack healing could be induced for a variety of materials. For the metallic materials considered in this study, the critical current densities are in the range of 0.3–0.6 A/mm^2, as shown in Figure 1-10.

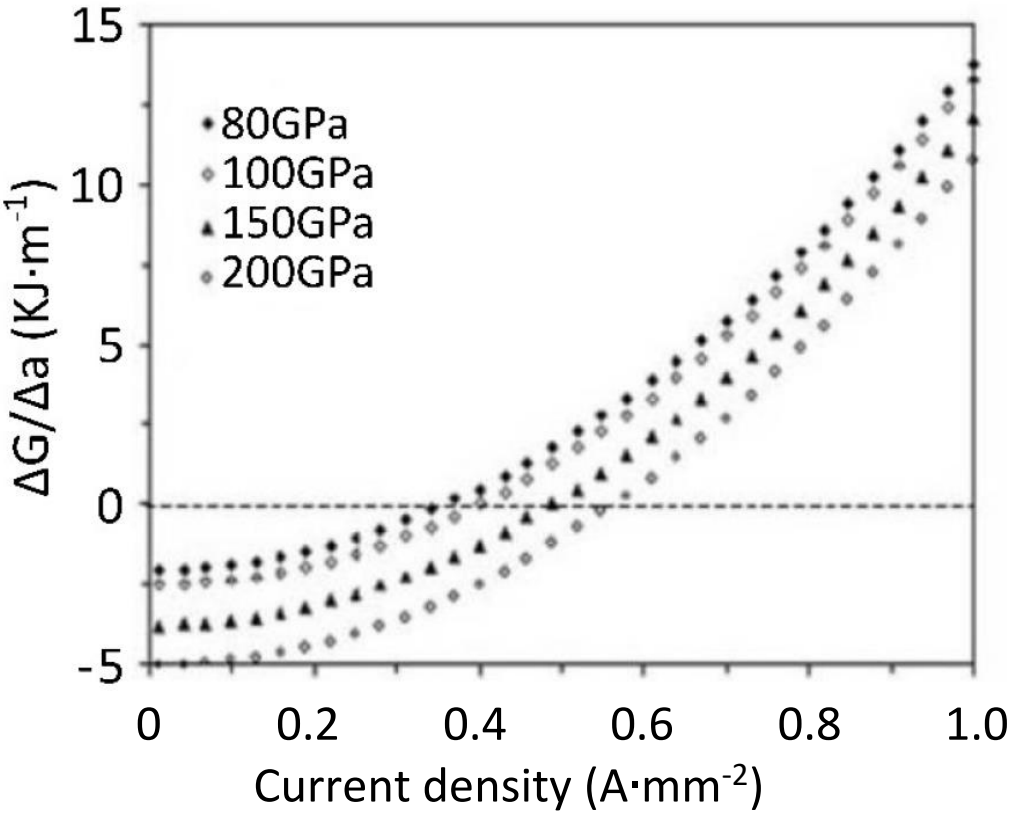

Figure **1-10**: Theoretical driving healing force during electropulsing treatment as a function of current density for various materials [136]. Modified from [4].

1.2.8. Mechanisms of Electropulsing Treatment

As of now, there is not a unified acknowledgement of the mechanisms behind EPT [3]. The multifactor theory coupling both thermal and athermal effects is currently the most accepted theory of the mechanisms behind EPT. Thermal effects of EPT include Joule heating, as well as the rate of heating and cooling, while athermal effects of EPT include the electron wind force (EWF), as well as the accumulation and annihilation of defects [3,4]. Numerous research has shown that EPT and Joule heating rates do not produce equivalent results, even when heating rate is equivalent. Furthermore, research has shown that there is a current density threshold that must

be surpassed, deemed a critical current density, to elicit changes in certain materials [4,146]. However, thermal and athermal effects of EPT are generally challenging to decouple, and ultimately, more research is necessary to completely understand the mechanisms behind EPT.

1.3. $Ti_3C_2T_x$ MXene

Since their discovery in 2011 [147,148], two-dimensional (2D) layered carbides and nitrides of transition metals, commonly referred to as MXenes, have become an emergent material in academic and industrial research due to their unique and advantageous properties [149–154]. These properties include an atomic-scale layered structure [148], high electrical conductivity [151,154–157], high thermal stability [158,159], mechanical properties of transition metal carbides and nitrides [151,154,160], efficient absorption of electromagnetic waves [154], hydrophilicity [154,155,158], and scalable processing methods [161]. With these properties, MXenes have shown to be useful in numerous energy storage, conversion, and electronic transport applications [151–153,156,162], including supercapacitors [151–153,163], batteries [152,153,163,164], electrodes for lithium-sulfur [152,153,165–168] and lithium-ion batteries [150–152,169–174], electromagnetic interference shielding [153,175–177], antennas and wireless communication [154,178], environmental and water treatment [153,179,180], various sensors [153,181,182], and even some biomedical applications [153,154,183]. More recently, MXenes have shown to be promising fillers for metal matrix composites [184–186] and ceramic matrix composites [186–188] by enhancing the electrical and mechanical properties of the matrices.

1.3.1. MXene Synthesis

MXenes are generally obtained through the removal of the intermediate element from their MAX phase precursor, which stems from the chemical formula of the precursor, $M_{n+1}AX_n$. In this formula, M denotes a transition metal (Ti, Zr, V, Nb or Mo), A denotes an A-group of elements primarily from groups 13–16 (Al, Ga, Si, Ge, P, or As), X denotes carbon (C) and/or nitrogen (N), and n denotes the layers of X. The MAX phase is a layered material with n+1 layers of M interleaved with n layers of X, where n = 1, 2, or 3 [156,189]. MXenes are obtained through the removal of the A-group layers of the MAX phase via selective etching, which are then replaced by surface functional groups or surface terminations due to the topochemical conversion from MAX to MXene [162]. Similar to their MAX phase precursors, MXenes are chemically denoted as $M_{n+1}X_nT_x$, where T_x denotes the surface group or termination. The most common surface groups or terminations are –OH, –O, –F, –Cl [156,162]. The surface functional groups or terminations [190] have shown to be critical in determining the electrochemical [151,190], magnetic [191], and electronic [174,191–193] properties of the MXenes. There are over 100 stoichiometric MXene compositions [154]. However, up to this point, over 70% of explored research on MXenes has been performed on $Ti_3C_2T_x$, which was the first discovered MXene [147,154]. $Ti_3C_2T_x$ is derived from the MAX phase Ti_3AlC_2 [147].

1.3.2. $Ti_3C_2T_x$ MXene Properties and Modifications

$Ti_3C_2T_x$ MXene has displayed unique and impressive material properties. Specifically, this MXene displays high electrical conductivity (up to 20,000 S cm^{-1}) [157], high thermal phase stability (up to 800 °C in non-oxidative environments) [159,194], high in-plane elastic stiffness (330±30 GPa) [160], and high colloidal stability (up to –40 mV in various solutions) [195,196].

While the properties of MXenes are quite impressive, there is a large gap between the theoretical capacitance and the capacitance obtained experimentally for these materials. There are two strategies that have been proposed in the literature to reduce this gap. The first is the optimization of the structure through alterations in interlayer spacing and surface terminations of the MXene itself. The second strategy is compounding the MXene with other materials, such as transition metal oxides, layered hydroxide nanosheets, and other carbon-based materials [155]. Within the first strategy, controllable surface modifications are crucial to maximize the potential performance MXenes, as the surface terminations are the primary factor that dictate the resulting properties. Numerous studies have shown advantageous surface and structural modifications of MXenes through thermal annealing and/or alkalinization and calcination [151,155,159,192,194,197–201]. HT of $Ti_3C_2T_x$ MXene has been performed from 150–1500 °C in varying environments.

1.3.3. Heat Treatment of $Ti_3C_2T_x$ in Non-Oxidative Environments

Although HT is an effective way to alter or remove surface terminations, $Ti_3C_2T_x$ and other titanium carbide MXenes are known to undergo structural oxidation and degradation when exposed to high temperatures in oxygen-containing environments [202–206]. This oxidation increases as the ambient temperature increases, and the oxidation leads to negative effects on the electrical conductivity of the MXene [202]. In order to avoid this oxidation and degradation, HT of MXenes has been performed in vacuums or inert environments [151,159,177,192–194,198,200,201,207].

In these non-oxidative environments, three regions or zones of HT have been identified for titanium carbide MXenes. The first region of annealing takes place from room temperature (RT) to 200 °C. In this region, interlayer water molecules within the MXene are lost

[151,192,194,208]. This interlayer water loss has resulted in up to an 18% decrease in sheet resistance for $Ti_3C_2T_x$ MXene at 200 °C [192]. The second region of HT takes place from 300–800 °C. In this region, the functional surface groups or terminations are desorbed and completely removed from the MXene [151,177,192,198,200,201,209]. Temperatures of 300–500 °C have resulted in the desorption of –OH [151,192,201], while temperatures of 500–750 °C have resulted in desorption of –F [192,201]. Further, temperatures of 800 °C or above result in complete removal of the surface groups [177,192,194,198,200,201]. The desorption and removal of the –F surface groups or terminations from $Ti_3C_2T_x$ has resulted in an approximate 75% decrease in electrical resistivity [192]. Additionally, this region of HT has also shown an increase in the thermal properties of titanium carbide MXene at 475 °C due to a reduction in interlayer spacing [207]. Lastly, the third region of HT takes place from approximately 800–1500 °C. This region leads to structural phase transformations from $Ti_3C_2T_x$ to mixed phases of Ti_2C and TiC_y, and eventually results in cubic TiC_y at 1500 °C [159,194]. Although the exact transition point from mixed crystalline Ti_2C and TiC_y to pure cubic TiC_y is unknown, it has been hypothesized that the transition occurs at 1000 °C [159]. Overall, conventional HT is an effective way to alter the properties of $Ti_3C_2T_x$, but the temperatures required lead to structural oxidation and degradation in ambient conditions [206].

1.3.4. Electron Wind Force Annealing of $Ti_3C_2T_x$ with Direct Current

In contrast to conventional HT, recently, electrical or EWF annealing has shown promise for improving MXene properties in ambient conditions without the need for a vacuum or inert environment [210]. Using EWF annealing with direct current (DC) and current densities up to 377 A/mm^2, a decrease in electrical resistivity of up to 72% was reported for $Ti_3C_2T_x$ MXene [210]. This 72% reduction is very comparable to the 75% reduction achieved with temperatures

up to 775 °C in a non-oxidative environment [192], but was achieved in ambient conditions with resulting temperatures only reaching 120 °C. Although temperatures only reached 120 °C, surface termination content, specifically =O, –H and –F, decreased, which occurred at a significantly lower temperature than in purely thermal annealing processes. It is hypothesized that EWF annealing is localized to the defects within the MXene, such as surface terminations and inter-flake defects, as opposed to thermal annealing processes, which are inherently more global.

In this study, a novel, non-thermal, RT annealing process is presented for $Ti_3C_2T_x$ MXene films that can achieve a larger reduction in electrical resistivity than previous HT and EWF annealing methods. This method is an EWF method that utilizes EPT, while simultaneously straining the MXene through compressive loading. This process is also shown to be largely permanent after compressive loading is removed. A group of samples was also annealed using exclusively EPT. Utilizing EPT minimizes the effect of Joule heating, provided that the proper parameters are selected. Minimizing Joule heating allows for the EWF to become the dominating effect for annealing. Furthermore, the process can be completed at RT, and therefore, can be completed in ambient environments without oxidation. Raman spectroscopy was utilized to analyze the composition and surface functional groups after EWF annealing. Focused ion beam (FIB) scanning electron microscope (SEM) surface and cross-section images were also utilized to analyze the structure and internal porosity after EWF annealing.

1.4. NiTi Shape Memory Alloy

Shape memory alloys (SMAs) are a class of multifunctional materials that react to stress, temperature, and other stimuli. As their name would imply, SMAs exhibit shape memory behavior, but also have the unique ability to withstand and recover from significantly more strain than other alloys without plastic deformation [211]. In addition, SMAs have other advantageous

functional properties, such as shape recovery rate, recovery stress, temperature range of shape recovery, transformation YS, and superelasticity [212–217].

There are numerous alloys with shape memory behavior, but nickel-titanium alloys, also commonly referred to as NiTi or Nitinol alloys, are the most prevalent. The increased ability for NiTi alloys to recover from strain is enabled by the reversible crystalline martensitic phase transformation between the B2 parent phase and B19' martensite phase [215,218–223]. Beyond shape memory and strain recovery properties of typical SMAs, NiTi alloys are also known for corrosion resistance [224,225], damping capacity [226], and biocompatibility with the human body [212,227,228]. Primarily, NiTi SMAs have applications in medical implants, staples, stents, and prosthetics [216,228], as well as orthodontic braces and stents [216,225,229–231]. In addition to biomedical applications, NiTi SMAs also have applications as actuators, and in architecture and structures [232].

1.4.1. Controlling Transition Temperature of Shape Memory Alloys

Before NiTi or any other SMAs can be used in these applications, the transformation temperature must be controlled or modified. This is because transformation temperature control for shape memory applications is often stringent. Traditionally, transformation temperatures of SMAs are controlled through composition control [233] or aging treatment [234]. Cold rolling (CR) with post-deformation thermal annealing is a common thermomechanical aging treatment for NiTi SMAs. The final HT is usually performed in environmental furnaces [235–239], and is used to refine the microstructure to obtain the desired martensitic transformation temperature and mechanical properties [214,240,241].

The effects of the final HT of NiTi SMAs are well documented [214,239] and have been used to produce NiTi with optimized mechanical and functional properties [236,242]. Thermal

annealing for this heat treatment is generally performed in the temperature range of 300–600 °C for 10–60 min, depending on the alloy composition and application [236,239]. The final heat treatment is also used to set the shape of the wire. If the shape of the NiTi is constrained during this annealing, stress is induced in the alloy temporarily [237,243]. Furthermore, in the manufacturing of superelastic NiTi wires, a constant tensile force, resulting in a stress of 20–100 MPa [236], is usually applied to achieve optimal properties [242].

1.4.2. Heat Treatment of NiTi

Aging through HT of NiTi has been studied extensively, even beyond the typical treatments of 300–600 °C for 10–60 min. Treated above the typical treatment temperatures, 55 at.% Ni–45 at.% Ti alloy was annealed between 400 and 1000 °C, and led to the observation of Ni_4Ti_3 and Ni_3Ti_2 metastable phases, as well as Ni_3Ti phase in equilibrium with the NiTi matrix phase. Ni_4Ti_3 and Ni_3Ti_2 phases have been shown to transform into Ni_3Ti when annealed for longer times and higher temperatures [244]. Treated above the typical treatment times, 50.7 at.% Ni–49.3 at.% Ti alloy was annealed at 500 °C for 60 min and 600 min. When annealed for 60 min, the alloy displayed lenticular Ni_4Ti_3 precipitates with an average diameter of 230 nm and thickness of 23 nm, which grows to an average diameter of 900 nm and thickness of 68 nm for a treatment time of 600 min [245]. In addition, interparticle spacing and volume fraction of precipitates have shown to increase with this increase in annealing time [245]. Treated around a similar temperature, 50.9 at.% Ni–49.1 at.% Ti alloy annealed at 560 °C displayed a single-stage transformation, indicating complete dissolution of Ni_4Ti_3 precipitate [246]. Lastly, treated below the typical treatment temperatures, 50.9 at.% Ni–49.1 at.% Ti alloy was annealed below 200 °C, which resulted in the suppression of the austenite-martensite transformation due to the formation of Guinier-Preston zone [246].

Ni_4Ti_3 and other precipitate observation is common in aging treatments of NiTi. Ni_4Ti_3 is also important in determining the functional properties of NiTi SMAs, as it will influence the B2–B19' martensitic phase transformation and R phase transformations [214]. In NiTi alloys that contain Ni_4Ti_3, smaller-sized precipitates appear closer to the grain boundaries than the grain interiors. Regardless, no field free of precipitates has been identified in the grain interiors. Coherent Ni_4Ti_3 precipitate induces strain field in the matrix, which aids in the R phase transformation during cooling [247].

1.4.3. Electron Wind Force Annealing of NiTi

Although aging through HT is common for NiTi, it is also very costly, inefficient, and increases lead time for these alloys. Additionally, NiTi alloy exposed to high temperatures for extended times can result in surface oxidation. More recently, EWF annealing has been used to age NiTi alloys due to lower overall processing cost, lower processing time, energy savings, and flexibility. EWF annealing with DC has been performed on 49.8 at.% Ni–50.2 at.% Ti alloy with current densities of 8.4–12.2 A/mm^2 for 60 min [248] and 50.8 at.% Ni–49.2at.% Ti with an approximate current density of 15.5 A/mm^2 for 10–600 s [249]. DC annealing has shown to be an effective method to shift the B2–R [248,249] phase transformation to lower temperatures and the R–B19' [248] phase transformation to higher temperatures. DC annealing has also led to the dissolution of Ni_4Ti_3 precipitate in aged NiTi alloy after a treatment time of 8 s [249].

However, similar to traditional thermal annealing, DC EWF annealing can cause irreversible structural variations, such as overgrowth of precipitates [245], or anneal to cold worked structures [250], due to overheating. These microstructural changes will alter the mechanical and functional properties of the alloy, as well as the transformation behavior [251,252].

1.4.4. Electropulsing Treatment of NiTi

One method to control and reduce overheating when performing electrical annealing is to utilize EPT. Numerous studies have performed EPT on NiTi alloys with varying degrees of initial deformation and aging, as well as varying electropulsing parameters [213,253–259]. As mentioned previously, EPT has often been performed during or immediately after rolling, referred to as EPR [253,254,256,259]. Generally, the EPT or EPR consists of peak current densities of 80–200 A/mm^2, pulse frequencies of 120–1000 Hz, and pulse widths of 80 µs, resulting in RMS current densities of 7–25 A/mm^2. However, RMS current density is not always reported. Total treatment time generally lasts a few seconds, as changes are induced much quicker than in traditional thermal annealing.

When performing purely EPT without rolling on NiTi alloy, studies have usually investigated the effects of one or more parameters beyond these typical values. Beyond the typical pulse widths, cold drawn 50.8 at.% Ni–49.2 at.% Ti underwent EPT with essentially singular pulses of very long pulse widths of 1000–18000 µs. Current densities were not reported. A maximum electrical resistivity reduction of 11.2% and maximum strain recovery of nearly 8% were achieved for samples annealed with pulse widths of 8000 and 12000 µs, respectively. Temperatures reached nearly 700 and 960 °C, respectively. The maximum strain recovery was enabled partially polygonized, partially recrystallized, microstructure with grain sizes of 25–50 nm [255]. Beyond the typical peak current densities and frequencies, cold rolled 44.16 at.% Ni–55.84 at.% Ti underwent EPT with very high peak current densities of 1625 A/mm^2, very high frequencies of 30000 Hz, and short pulse widths of 4.3–5.8 µs, for a total treatment time of 8 s. These parameters resulted in RMS current densities of 585.6–665.8 A/mm^2. The martensite transformation temperatures and superelasticity were found to increase, while hardness was found to decrease, with increasing current density. A maximum hardness reduction of nearly 25% was

achieved for the pulse width of 5.8 µs. After EPT, the microstructure consisted predominantly of B2 phase with trace amounts of B19' phase [257]. Lastly, beyond the typical treatment times, thermally annealed 50.8 at.% Ni–49.2 at.% Ti underwent EPT with peak current densities of 95–114 A/mm^2, frequencies of 150–350 Hz, and pulse widths of 80 µs, for a treatment time of 2.5–15 min. These parameters resulted in RMS current densities of 7.83–9.38 A/mm^2 [213,258]. Maximum temperatures of the samples reached 325, 380, and 420 °C, for frequencies of 150, 250, and 350 Hz, respectively. The NiTi samples displayed up to 8% fully recoverable strain [213], nearly a 20% decrease in electrical resistance [213,258], and just over a 30% reduction in hardness [258] after EPT. The band microstructure with an average width of 41 nm was transformed into an equiaxed grain microstructure, where the grains increased in size from 250 nm to 1.95 µm as frequency and treatment time increased. All samples that underwent EPT contained Ti_3Ni_4 precipitate, but as frequency increased to 350 Hz, Ni_3Ti precipitate was also observed [213]. In all of these studies, the thermal and mechanical changes in NiTi alloys after EPT were attributed to decreasing dislocation density due to EWF [213,255,257,258].

1.4.5. Electropulse Rolling Treatment of NiTi

Numerous studies have performed EPR to significantly increase deformability and plasticity of NiTi alloy [253,254,256,259]. First, 50.7 at.% Ni–49.3 at.% Ti underwent EPR consisting of peak current densities of 80 A/mm^2 and up to 240 A/mm^2, frequencies of 1000 Hz, and pulse widths of 80 µs. This EPR increased deformability and decreased hardness. It was found that higher current densities during EPR lead to less crack initiation. Current density and the degree of plastic deformation were determined to be the most critical factors for altering the microstructure [253]. Second, hot rolled 50.7 at.% Ni–49.3 at.% Ti underwent EPR consisting of a rolling rate of 0.035 m/s, peak current densities of 84–168 A/mm^2, frequencies of 1000 Hz,

pulse widths of 80 and 160 μs, and deformations of 0.77–1.81. EPR resulted in a significant increase in the deformability, with current density playing the most significant role and pulse width playing a smaller role. A maximum deformation before fracture of 1.7–1.8 was reported for the maximum current density and pulse width, compared to a maximum of 0.5–0.6 for CR alone. After EPR and post deformation annealing (PDA) at 400 °C, a homogenous nanocrystalline grain structure was achieved with an average grain size of 100 nm [254]. Third, cold rolled 50.8 at.% Ni–49.2 at.% Ti underwent EPR consisting of peak current densities of 135.8–193.9 A/mm^2, frequencies of 120–500 Hz, and pulse widths of 80 μs, resulting in RMS current densities of 11.0–18.9 A/mm^2. Maximum temperatures during the process ranged from 145–450 °C. The NiTi alloy took just 9 s to complete recrystallization. This EPR resulted in a maximum electrical resistivity reduction of 13.6% and maximum strain recovery of 6.94%. The NiTi microstructure transformed from martensite lath structures with an average width of 41 nm to nanograins with an average size of 10–20 nm after a frequency of 300 Hz. Furthermore, the nanograins grew to an average grain size of 100–200 nm after EPT with 500 Hz [256]. Lastly, 50.8 at.% Ni–49.2 at.% Ti underwent EPR consisting of peak current densities of 132.1–189.9 A/mm^2, frequencies of 120–500 Hz, pulse widths of 80 μs, and rolling reduction percentages of 22.7–30.3%. These parameters resulted in RMS current densities of 13.0–25.2 A/mm^2, and temperatures ranging from 120–600 °C. Sample elongation increased drastically from 6.0% for CR alone up to 26.8% for the EPR condition. Hardness reduced 12.0% from 424 HV_1 down to 373 HV_1. For CR alone, NiTi alloy easily becomes brittle and develops cracks, especially as reduction percentage increases. EPR of NiTi can enhance the ductility and decrease the resistance of deformation during rolling [259].

Although there are numerous studies investigating EPT and EPR of NiTi SMA, no studies have investigated a broad range of electropulsing parameters, such as frequency and pulse width, and the resulting RMS current densities. Widening or broadening the range of parameters

allows for optimization of the electropulsing process for NiTi. Furthermore, no studies have investigated low-temperature EPT of NiTi, in which temperatures fall below 325 °C. In this study, 50.7 at.% Ni–49.3 at.% Ti SMA wire undergoes EPT consisting of peak current densities of 157.4–601.7 A/mm^2, frequencies of 2–160 Hz, and pulse widths of 40–5000 μs, resulting in RMS current densities of 3.9–43.0 A/mm^2. Temperatures generally fall below 325 °C. Electrical resistivity was measured pre- and post-EPT to assess magnitude of change.

Chapter 2

Experimental Methods

The following sections will detail the experimental materials and methods utilized throughout the low-temperature electropulsing experiments. The first section will detail the general experimental setup for all EPT, while the second and third sections will detail specific experimental setups, as well as characterization techniques, for $Ti_3C_2T_x$ MXene and NiTi SMA, respectively.

2.1. General Experimental Setup

A Northrop Grumman eDrive laser system controller diode-based pulsing instrument was utilized to generate pulsed DC (electropulses). The eDrive was powered by a Sorensen DCS 100-12E power supply set to 20 V DC. The electrical signal generated by the eDrive was characterized using a Rigol DS 1104 oscilloscope. The eDrive was also used to sense the electrical current during EPT. This sensed current was used to calculate the resulting current densities through the samples during EPT. The electrical signal generated for EPT, as well as duration of EPT, varied based upon material and sample, and will be detailed in the following subsections.

Electrical resistance pre- and post-EPT was determined from a current-voltage (I-V) curve, which was supplied and measured with a Keithley 2400 source measurement unit. Resistance was converted to resistivity by multiplying with the constant cross-sectional area and dividing by the length of the sample. For all measurements, Kelvin connections were utilized to minimize contact resistance. All resistivity measurements were performed at room temperature (RT) to avoid errors due to thermal expansion or thermal coefficient of resistivity.

Temperature and thermal changes during the process of EPT were measured using an Optris PI 640i thermal IR imaging camera. The Optris PI 640i uses a focal plane array, uncooled, 17 × 17 µm detector with an optical resolution of 640 × 480 pixels, a spectral range of 7.5–13 µm, a temperature range of –20–900 °C, a frame rate of 32 Hz/125 Hz at 640 × 120 pixels, a thermal sensitivity or noise equivalent temperature distribution of 40 mK, and has a system accuracy of ±2 °C or ±2% at ambient temperature. A schematic diagram of this general experimental setup for EPT is shown in Figure 2-1.

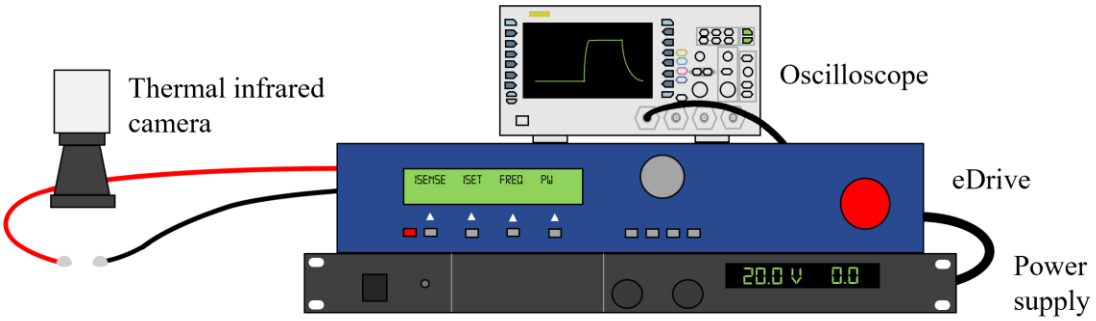

Figure **2-1**: Schematic of general experimental setup for electropulsing treatment.

2.2. $Ti_3C_2T_x$ MXene

The pristine as-received $Ti_3C_2T_x$ MXene film was obtained in a 46 mm diameter and thickness of 500 µm from Nanochemazone, as shown in Figure 2-2. The following subsections describe the $Ti_3C_2T_x$ sample preparation for EWF annealing, the specific experimental setup, as well as the characterization techniques of Raman spectroscopy, and FIB SEM.

Figure **2-2**: Pristine as-received $Ti_3C_2T_x$ MXene film of 46 mm diameter and 500 µm thickness.

2.2.1. $Ti_3C_2T_x$ Sample Preparation

The $Ti_3C_2T_x$ film was processed into approximately 4 mm × 3 mm rectangles for EWF annealing. The samples were mounted to card stock substrates, as a low thermal conductivity substrate (approximately 0.05 W/mK) is suitable for the annealing process. Electrical connections were made with silver epoxy.

2.2.2. $Ti_3C_2T_x$ Experimental Setup

For $Ti_3C_2T_x$ MXene experiments, the electrical signal generated from the eDrive consisted of a peak current of up to 15 A, frequency of 2 Hz, and pulse width of 40 µs. EPT was

performed for up to 240 seconds for $Ti_3C_2T_x$ MXene samples. A visual representation of the electrical signal is shown in Figure 2-3.

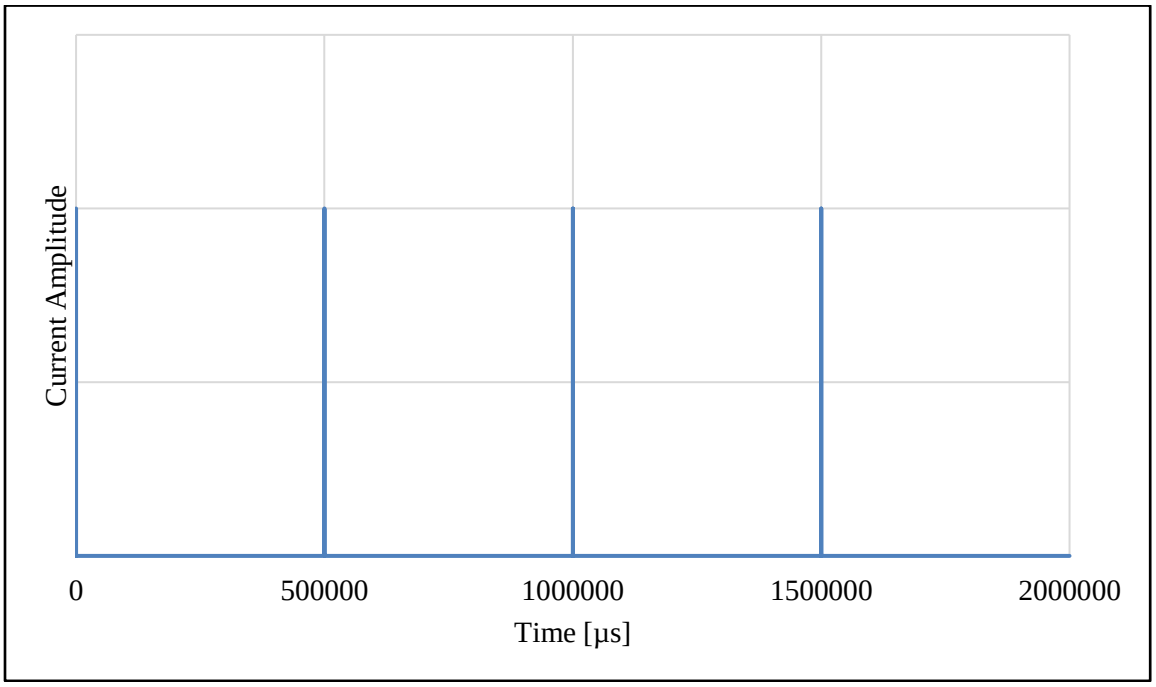

Figure **2-3**: Electrical signal generated for electron wind force annealing of $Ti_3C_2T_x$ MXene.

To compress the $Ti_3C_2T_x$ MXene samples during EPT, an adapter was manufactured through AM or 3D printing. This adapter was used to concentrate a 2.246 kg mass down to a 3 mm wide distance that was placed on top of the samples. The adapter had a mass of 20 g. This experimental set up resulted in a total mass of 2.266 kg that was concentrated down to the 3 mm wide surface. A schematic diagram of this experimental setup for EWF annealing is shown in Figure 2-4.

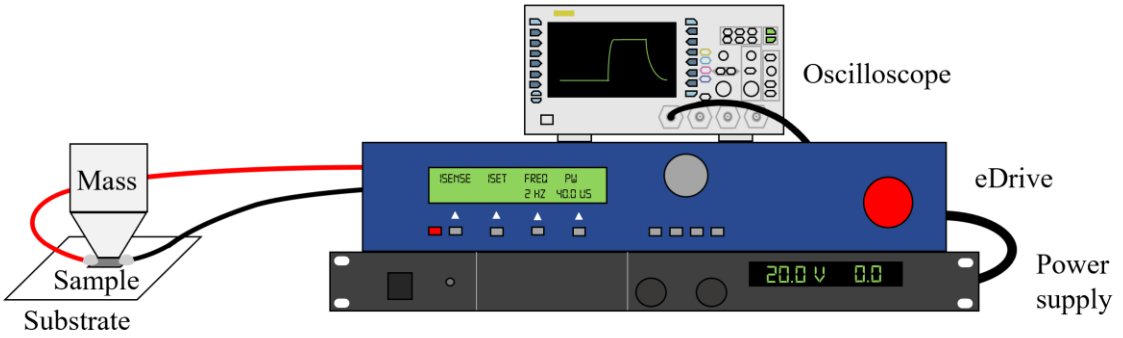

Figure **2-4**: Schematic of experimental setup for electron wind force annealing process of $Ti_3C_2T_x$ MXene with electropulsing and compression.

It is important to note that due to the experimental setup shown in Figure 2-4, IR thermal imaging was not performed for samples that underwent compressive loading, and was only performed for samples that underwent exclusively EPT. A schematic diagram of the experimental setup for exclusively EPT is shown in Figure 2-5.

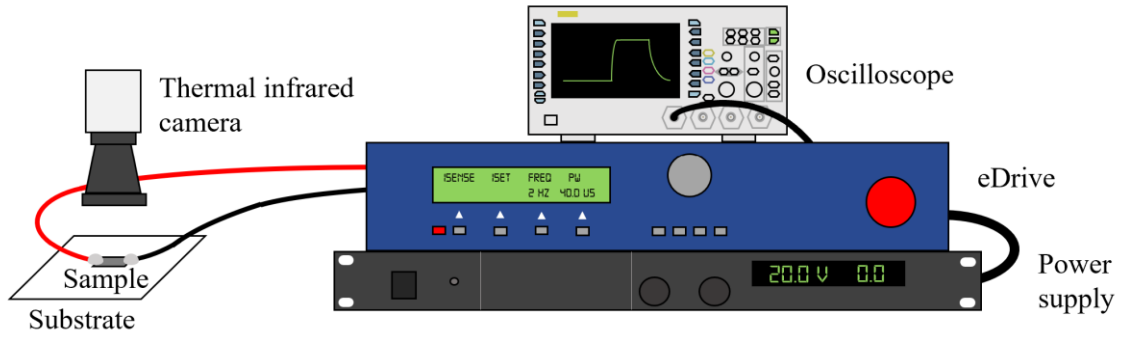

Figure **2-5**: Schematic of experimental setup for electron wind force annealing process of $Ti_3C_2T_x$ MXene with exclusively electropulsing treatment.

2.2.3. $Ti_3C_2T_x$ Raman Spectroscopy

Raman spectroscopy is a useful non-destructive evaluation tool, which can be used to investigate the crystal structure and phonon vibration within 2D materials, such as MXenes. For $Ti_3C_2T_x$ MXene, Raman spectroscopy has been used to determine composition, phase stability, and in some cases, spectral response has been linked to physical properties of MXene materials [260]. In this study, the research team used a Horiba LabRam HR Evolution instrument with a 50 × long working distance objective with a numerical aperture of 0.5. An average Duoscan spot size diameter of 20 µm was utilized to reduce effective power density of the laser, as well as to increase the measured Raman spectral response. Raman spectral data was obtained with a 785 nm wavelength laser with laser power maintained at approximately 1.7 mW, a 300 gr/mm grating, and a confocal hole size of 200 µm. Acquisitions were recorded with 60 s integration and 3 accumulations. Lorentzian peak fitting of Raman spectral data was performed in Origin software. A minimum of 3 locations were recorded from each sample.

2.2.4. $Ti_3C_2T_x$ Focused Ion Beam Scanning Electron Microscopy

Surface and cross-sectional images of the $Ti_3C_2T_x$ MXene samples were taken pre- and post-EWF annealing using a FIB SEM. The cross-sectional milling was performed using FEI Helios NanoLab 660 dual beam SEM with a Gallium ion source. The acceleration voltage of the ion beam was set to 30 kV during milling. Rough milling was performed with a current of 65 nA to remove the material, while the polishing of the cross-sectional wall was performed with a current of 2 nA. Surface SEM images were taken using a typical electron beam with a magnification of 8000 ×. Cross-sectional SEM images were taken with a typical electron beam at

a tilt angle of 52° and magnification of 20000 ×. A tilt correction feature was utilized to maintain the aspect ratio of the images.

2.3. NiTi Shape Memory Alloy

50.7 at.% Ni–49.3 at.% Ti wire in 0.5 mm diameter was obtained from Kellogg's Research Labs. Prior to EPT, the wire was cold drawn to an area reduction of approximately 30% and an UTS of 785 MPa. The transformation temperature of the obtained wire was 80 °C, which is classified as a high transformation temperature. The following subsections describe the NiTi sample preparation for EPT and the specific experimental setup for EPT of NiTi.

2.3.1. NiTi Sample Preparation

To perform EPT, the wire was processed into lengths of approximately 30 mm. Electrical connections were made with standard alligator clips.

2.3.2. NiTi Experimental Setup

For NiTi SMA experiments, the electrical signal generated from the eDrive consisted of a peak current of 27–104 A, frequency of 2–160 Hz, and pulse width of 40–5000 µs. EPT was performed for 180 s for all NiTi samples. A schematic diagram of the experimental setup for EPT is shown in Figure 2-6.

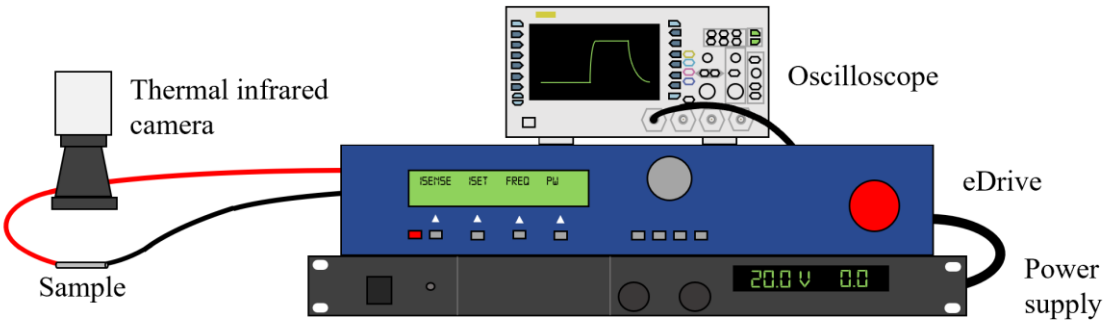

Figure **2-6**: Schematic of experimental setup for electropulsing of NiTi shape memory alloy.

Chapter 3

Experimental Results

The following sections describe and illustrate the experimental results for EPT of $Ti_3C_2T_x$ MXene and NiTi SMA, respectively.

3.1. $Ti_3C_2T_x$ MXene

The following subsections illustrate the results of EPT on $Ti_3C_2T_x$ MXene through electrical resistivity, IR thermal imaging, Raman spectroscopy, and FIB SEM.

3.1.1. $Ti_3C_2T_x$ Electrical Resistivity

Utilizing this EWF annealing process consisting of EPT and compressive loading, a maximum resistivity reduction of 96.65% was achieved for $Ti_3C_2T_x$ MXene. This reduction was achieved for $Ti_3C_2T_x$ sample C1 with a maximum sensed current of 12.2 A, resulting in an approximate peak current density of 7.4 A/mm^2, after 240 seconds of EWF annealing. When the post-annealing resistivity measurement was repeated over 24 hours later, the resistivity increased back slightly, but the resulting reduction was still measured to be 94.80% from the pre-annealing resistivity. This result indicates that the EWF annealing process is partially, but not completely permanent. Table 3-1 displays a summary of the EWF annealing data for this process. The assignment C denotes a sample that underwent EPT and compressive loading. $Ti_3C_2T_x$ samples C1–C3 all displayed over a 90% reduction in resistivity when measured immediately after EWF annealing. All $Ti_3C_2T_x$ samples displayed a slight increase in resistivity when measured over 24

hours later, which indicates that the process is not completely permanent and is time-dependent. Unfortunately, a repeated resistivity measurement for $Ti_3C_2T_x$ sample C3 was unable to be performed due to a lost electrical connection.

Table **3-1**: $Ti_3C_2T_x$ sample C1–C6 data for electron wind force annealing process consisting of electropulsing treatment and compressive loading.

Sample	Pre-Annealing Resistivity [Ohm-m]	Immediate Post-Annealing Resistivity [Ohm-m]	Immediate Resistivity Reduction [%]	Repeated Post-Annealing Resistivity [Ohm-m]	Repeated Resistivity Reduction [%]
C1	3.518E-02	1.180E-03	96.65%	1.829E-03	94.80%
C2	1.252E-02	5.535E-04	95.58%	7.518E-04	94.00%
C3	3.704E-02	3.299E-03	91.09%	-	-
C4	1.636E-02	2.049E-03	87.48%	5.646E-03	65.48%
C5	4.120E-03	7.253E-04	82.40%	1.003E-03	75.65%
C6	3.065E-03	1.141E-03	62.78%	1.718E-03	43.93%

For $Ti_3C_2T_x$ samples that underwent the annealing process consisting of exclusively EPT, the maximum resistivity reduction was 77.96%. This reduction was achieved for $Ti_3C_2T_x$ sample E1 with a maximum sensed current of 9.4 A, resulting in an approximate peak current density of 10.4 A/mm^2, after 240 seconds of annealing. Table 3-2 displays a summary of the EWF annealing data for this process. The assignment E denotes a $Ti_3C_2T_x$ sample that underwent exclusively EPT. As mentioned previously, this reduction can be improved with the addition of compressive loading. It is also important to note that this process is permanent and is not time-dependent.

Table **3-2**: $Ti_3C_2T_x$ sample E1–E8 data for electron wind force annealing process consisting of exclusively electropulsing.

Sample	Pre-Annealing Resistivity [Ohm-m]	Post-Annealing Resistivity [Ohm-m]	Resistivity Reduction [%]	Maximum Temperature [°C]
E1	2.367E-03	5.217E-04	77.96%	30.7
E2	1.788E-03	5.369E-04	69.96%	26.0
E3	2.123E-04	7.024E-05	66.91%	27.0
E4	7.372E-05	3.151E-05	57.25%	27.2
E5	2.182E-05	1.030E-05	52.77%	27.6
E6	9.194E-05	4.613E-05	49.83%	29.6
E7	9.577E-04	4.999E-04	47.80%	27.0
E8	2.915E-03	1.561E-03	46.45%	29.2

3.1.2. $Ti_3C_2T_x$ Infrared Thermal Imaging

An advantage of utilizing EPT for EWF annealing, as opposed to DC, is that the annealing process can be performed at significantly lower temperatures, as shown in Table 3-2. Figure 3-1 illustrates the maximum temperature recorded of 30.7 °C for $Ti_3C_2T_x$ sample E1. Figure 3-2 illustrates the maximum temperature recorded of 26.0 °C for $Ti_3C_2T_x$ sample E2. These samples indicate that this annealing process can be completed at RT. Because the electrical signal for this process and the process including compressive loading are identical and current densities are very similar, it is safe to assume that the process with compressive loading can also be completed at RT.

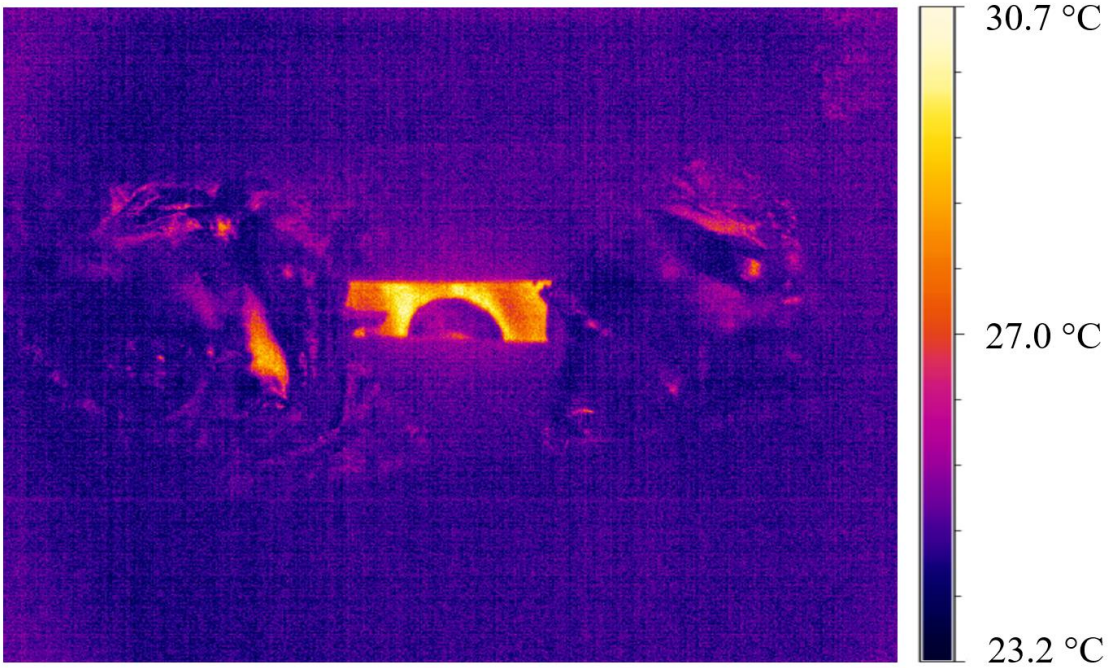

Figure **3-1**: Infrared thermal image of $Ti_3C_2T_x$ sample E1 during electropulsing that resulted in a 77.96% reduction in resistivity and maximum temperature of 30.7 °C.

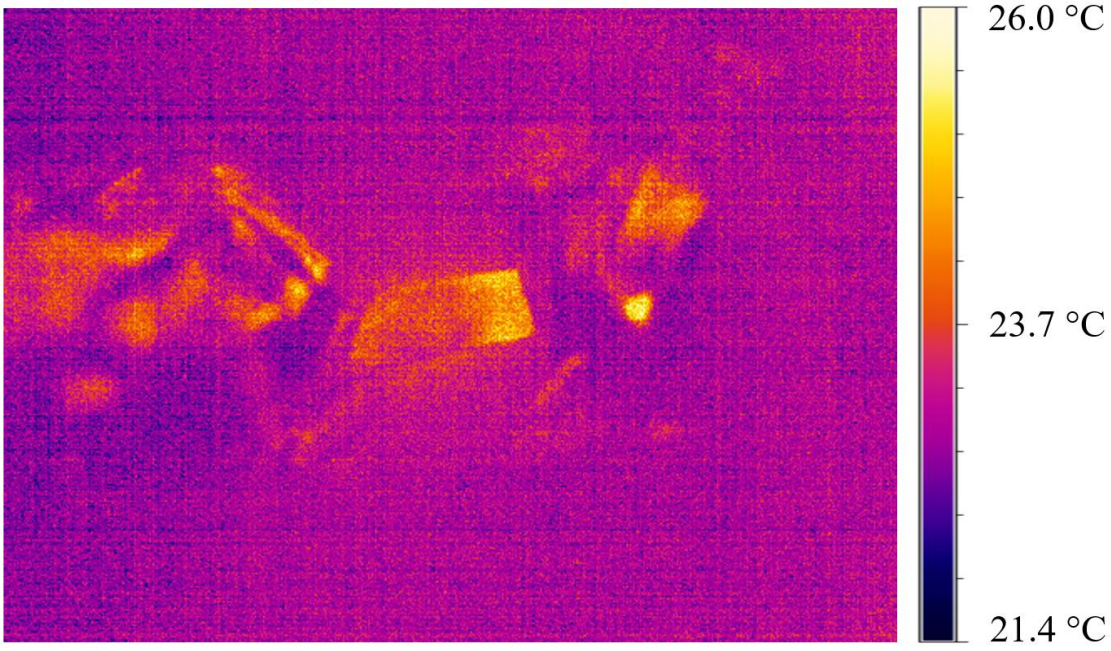

Figure **3-2**: Infrared thermal image of $Ti_3C_2T_x$ sample E2 during electropulsing that resulted in a 69.96% reduction in resistivity and maximum temperature of 26.0 °C.

3.1.3. $Ti_3C_2T_x$ Raman Spectroscopy

Raman analysis with 785 nm excitation laser provides access to the plasmonic resonance enhanced Raman modes ω_1: 123 cm^{-1} (E_g, Ti2-C in-plane mode), ω_3: 728 cm^{-1} (A_{1g}, C out-of-plane mode), and ω_6: 513 cm^{-1} (A_{1g}, T_x out-of-plane mode) [261]. Examination of the changes in the Raman spectral response between the as-received MXene and EWF annealed specimen in Figure 3-3 shows the ω_1 and ω_3 peak maximum positions are unchanged after annealing. However, the full width at half maximum (FWHM) is increased (< 0.1 cm^{-1}) as indicated by small peaks in the residual spectrum. The ω_1 and ω_3 peak positions have been determined to be sensitive to the type of surface terminated functional group [261]. Therefore, within the sensitivity of Raman spectroscopy, no modification to the composition of T_x species is identified post-EWF annealing.

The notable difference in the Raman spectroscopy post-EWF annealing is the increase in the relative signal amplitude for the ω_4–ω_7 modes, all of which are associated with T_x vibrations [262]. This relative increase in signal intensity of the ω_4–ω_7 modes can be attributed to an increase in the T_x concentration within the volume analyzed [260]. A time dependence study of the as-received MXene specimen, measured 1 month later, also shows an increase in the ω_4–ω_7 mode intensities, with < 1/3 signal increase measured in the EWF annealed samples. In summary, the changes in the structure and composition of the EWF annealed MXene samples as determined by Raman spectroscopy are minimal, with only a moderate change in overall T_x concentration.

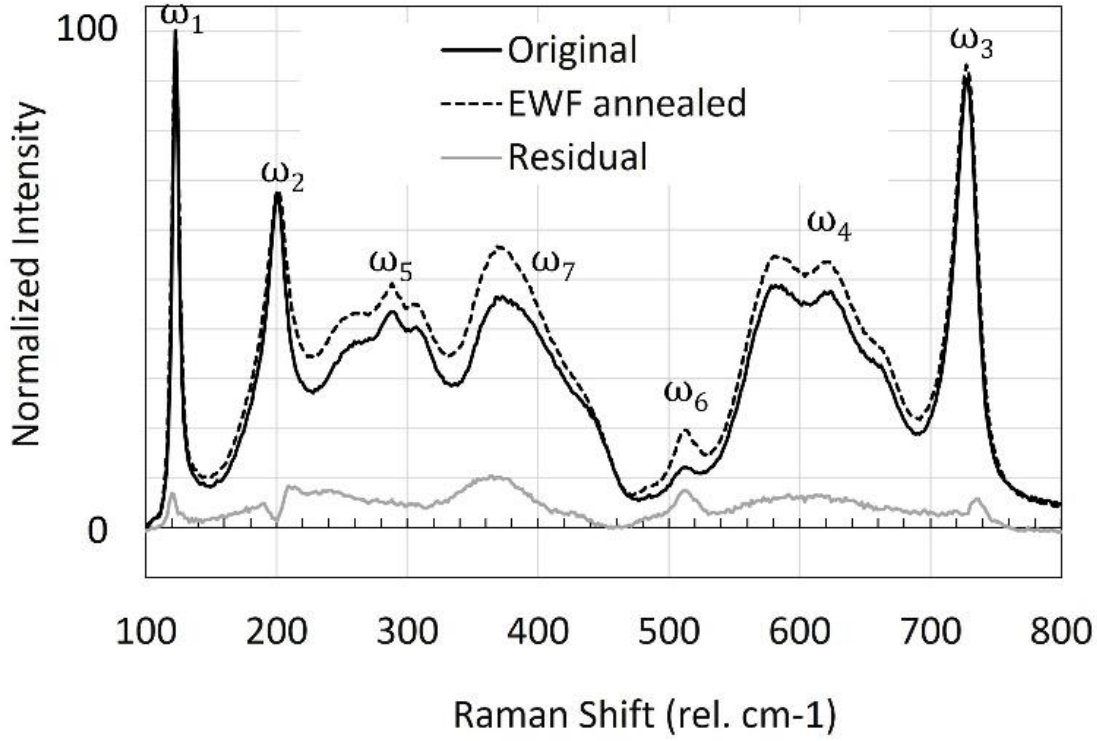

Figure **3-3**: Raman spectral averaged response from the original as-received MXene sample compared with the average response of all electron wind force annealed samples and normalized to the ω_1 resonance peak at 123 cm^{-1}. The residual response depicted is a result of the electron wind force annealed spectrum minus the original spectrum.

3.1.4. $Ti_3C_2T_x$ Focused Ion Beam Scanning Electron Microscopy

Surface and cross-sectional FIB SEM images were taken for the as-received $Ti_3C_2T_x$ MXene, as well as for samples C2, C3, E1, and E2. As mentioned previously, surface images were taken at a magnification of 8000 ×, while the cross-sectional images were taken at a magnification of 20000 ×. As FIB SEM is a destructive technique, images of the same sample could not be taken pre- and post-EWF annealing.

Surface SEM images can be viewed in Figure 3-4. Figure 3-4a displays the as-received sample, while Figure 3-4b, 3-4c, 3-4d, and 3-4e display samples C2, C3, E1, and E2, respectively.

Although there is variation in samples, there is no apparent visual difference in surface roughness or surface structure after EWF annealing.

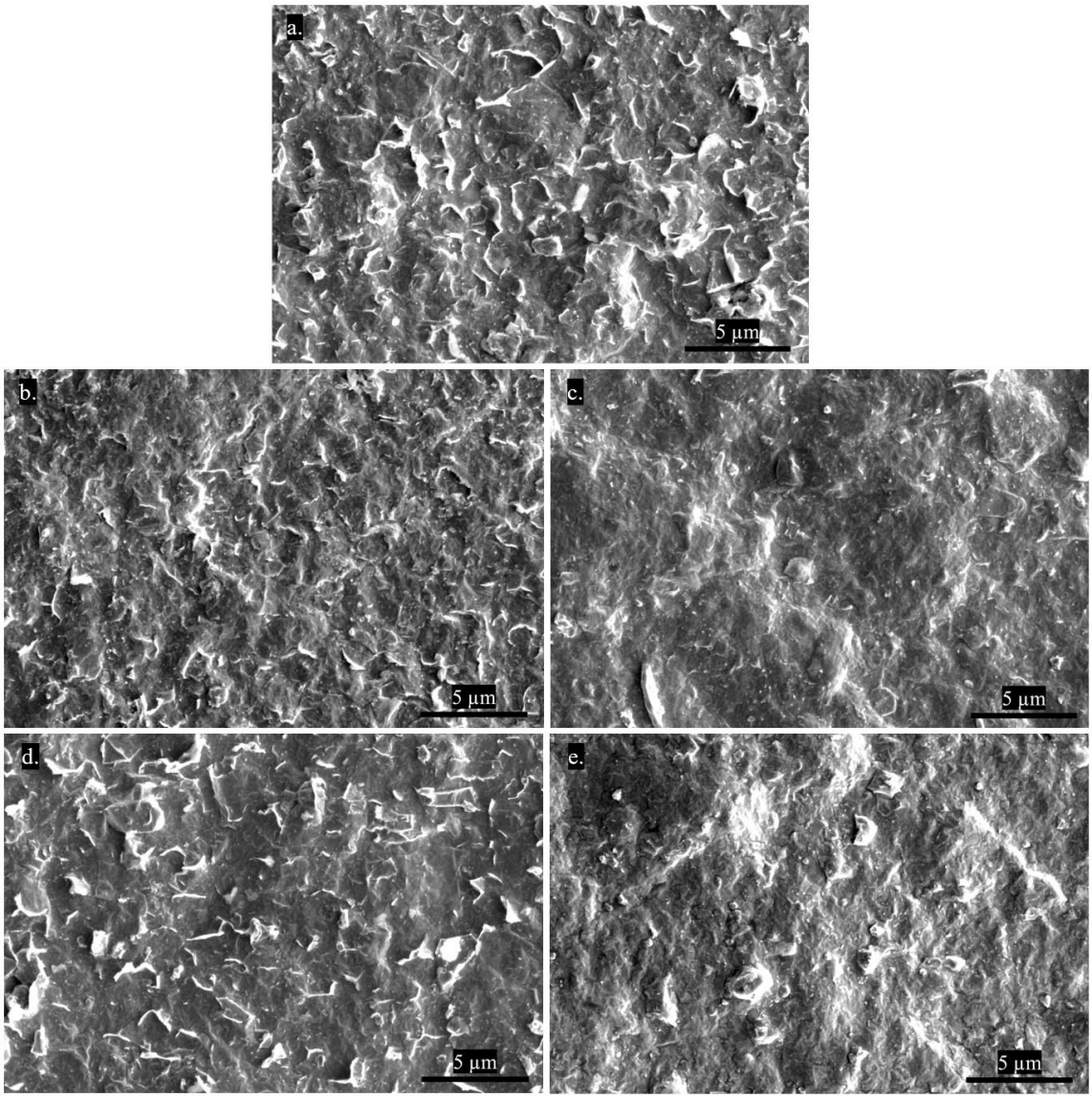

Figure **3-4**: $Ti_3C_2T_x$ surface scanning electron microscope images of, **a.** as-received sample, **b.** sample C2, **c.** sample C3, **d.** sample E1, and **e.** sample E2.

Because the same samples could not be compared pre- and post-EWF annealing, an analysis of internal pore size was performed for each cross-sectional FIB SEM image utilizing ImageJ software and compared to the as-received sample. A summary of the porosity analysis can be viewed in Table 3-3. The cross-sectional FIB SEM images and the corresponding internal pore size histograms can be viewed in Figure 3-5. Figure 3-5a displays the as-received sample, while Figure 3-5b, 3-5c, 3-5d, and 3-5e display samples C2, C3, E1, and E2, respectively. Cross-sectional images were processed in ImageJ by cropping to a 12–14 μm^2 area of constant illumination, applying a bandpass filter, and thresholding the shades to locate the internal pores, which corresponded to the darkest 13–15% of shades. As shown in Table 3-3, the porosity volume fraction for all EWF-annealed samples decreased slightly when compared to the as-received sample. The as-received sample had a porosity volume fraction of approximately 14.4%, while sample E2 displayed the lowest porosity volume fraction of 12.1%. Additionally, the average internal pore size for all EWF-annealed samples decreased when compared to the as-received sample. The as-received sample displayed an average internal pore size of 2163 nm^2, while sample C3 displayed the smallest average internal pore size of 1515 nm^2. Furthermore, Figure 3-5 showcases the normalized frequency of the internal pore sizes for each sample. There is a drastic shift from medium-to-large-sized pores in the as-received sample down to small-sized pores in the EWF-annealed samples. This is evident based on the normalized frequency of the smallest 0–600 nm^2 pore size. For the as-received sample, 26.1% of pores had an area of 0–600 nm^2. For the EWF-annealed samples, 30.1–38.8% of pores displayed an area of 0–600 nm^2, with the largest percentage coming from sample C2. Generally, there is a decrease in all medium-to-large-sized pores from the as-received to EWF-annealed samples, with the largest reduction coming from medium-sized pores with an area of approximately 3000–6000 nm^2. Although there is only a minor change in porosity volume fraction, it is evident that there is a drastic change in

the frequency of nearly all pore sizes, resulting in a smaller average internal pore size after EWF annealing.

Table **3-3**: Summary of $Ti_3C_2T_x$ internal porosity analysis.

Sample	Resistivity Reduction [%]	Porosity Volume Fraction [%]	Average Pore Size [nm^2]	Sample Standard Deviation [nm^2]
As-received	N/A	14.4%	2163	2858
C2	95.58%	13.1%	1994	5119
C3	91.09%	13.2%	1515	2095
E1	77.96%	12.8%	2014	4210
E2	69.96%	12.1%	1982	2372

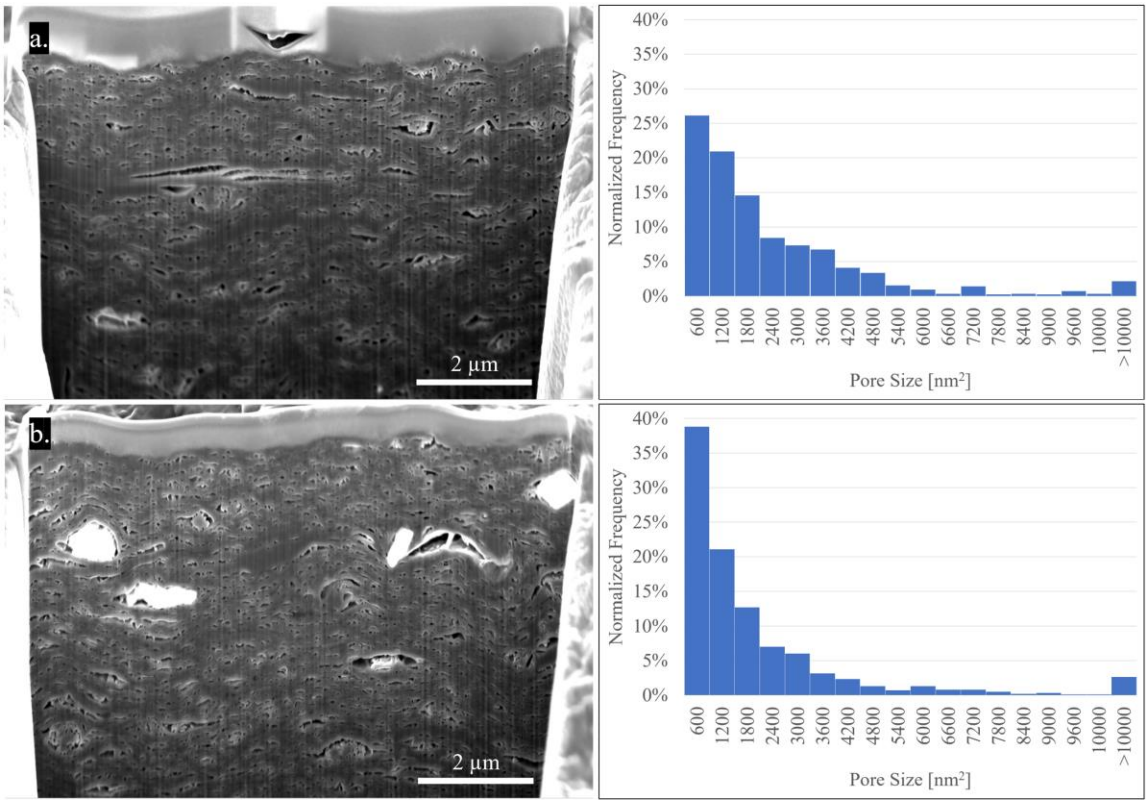

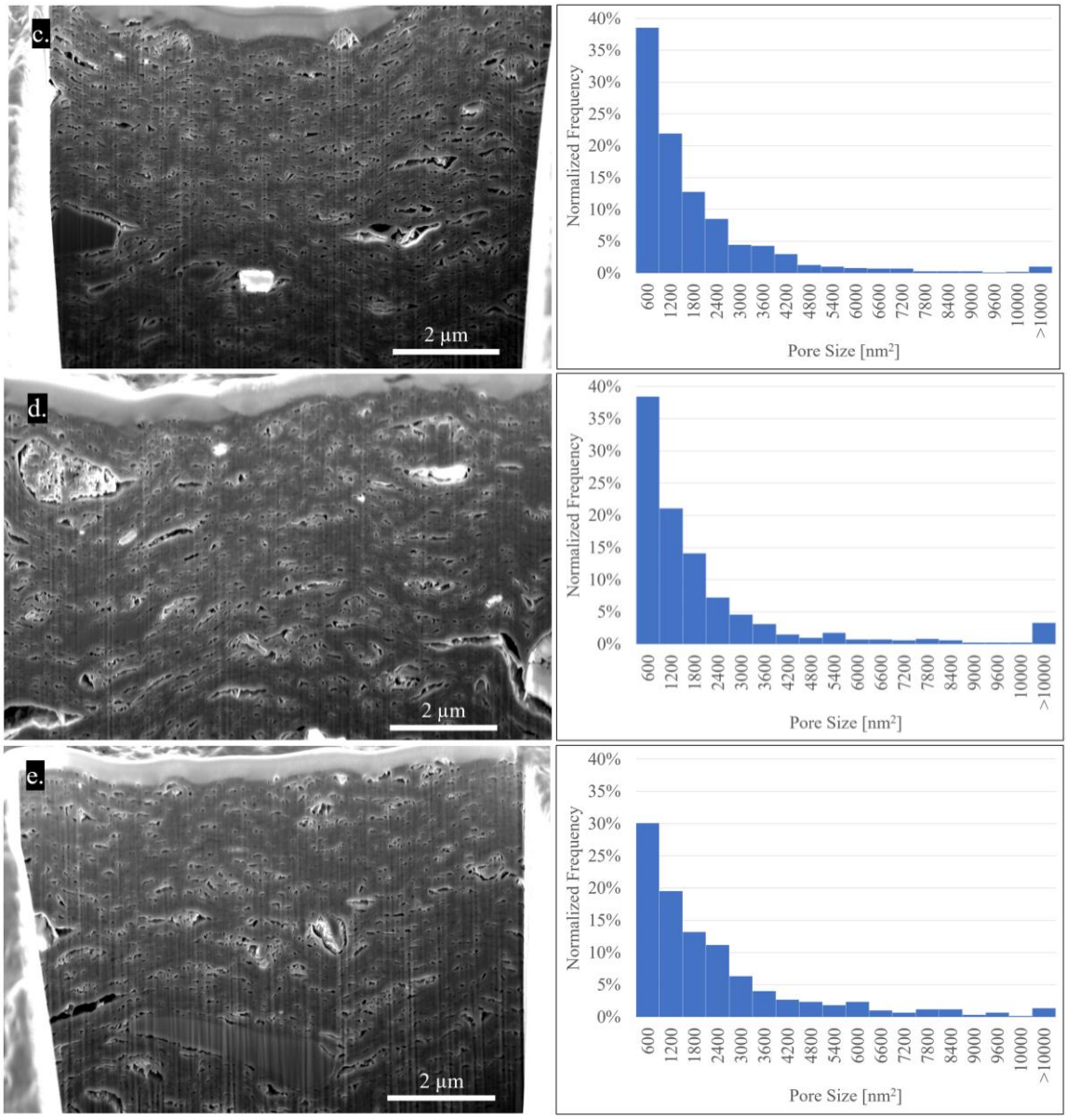

Figure **3-5**: $Ti_3C_2T_x$ cross-sectional focused ion beam scanning electron microscope image and corresponding internal pore size histogram of, **a.** as-received sample, **b.** sample C2, **c.** sample C3, **d.** sample E1, and **e.** sample E2.

3.2. NiTi Shape Memory Alloy

The following subsections illustrate the results of EPT on NiTi SMA through electrical resistivity and IR thermal imaging.

3.2.1. NiTi Electrical Resistivity

In an attempt to optimize the parameters of EPT, NiTi samples 1–17 investigated low frequency and high pulse width, while NiTi samples 18–28 investigated high frequency and low pulse width. Peak current density was maintained as high as possible because that has proven to be the primary factor in eliciting microstructure and property change [4]. However, peak current density did fall for NiTi samples 4–17 due to machine limitations. A summary of EPT results can be viewed in Table 3-4. By varying the parameters of EPT to optimize the changes in NiTi SMA, a maximum electrical resistivity reduction of 8.11% was achieved. NiTi sample 15 displayed this 8.11% reduction after EPT consisting of a peak current density of 179.3 A/mm^2, a frequency of 2 Hz, and a pulse width of 4000 μs, resulting in an RMS current density of 16.0 A/mm^2. Another close resistivity reduction of 7.58% was displayed by NiTi sample 25. NiTi sample 25 underwent EPT consisting of peak current density of 533.2 A/mm^2, a frequency of 100 Hz, and a pulse width of 40 μs, resulting in an RMS current density of 33.7 A/mm^2.

Table **3-4**: Summary of electropulsing results for NiTi samples 1–28.

Sample	Pre-EPT Resistivity [Ohm-m]	Peak Current Density [A/mm^2]	Frequency [Hz]	Pulse Width [µs]	RMS Current Density [A/mm^2]	Total Duration [s]	Post-EPT Resistivity [Ohm-m]	Resistivity Reduction [%]	Maximum Temperature [°C]
1	1.825E-06	432.9	2	40	3.9	180	1.816E-06	0.49%	30
2	2.366E-06	582.2	2	250	13.0	180	2.312E-06	2.25%	63
3	2.073E-06	522.2	2	500	16.5	180	2.023E-06	2.42%	93
4	2.242E-06	488.8	2	750	18.9	180	2.155E-06	3.88%	177
5	2.521E-06	484.7	2	1000	21.7	180	2.430E-06	3.62%	202
6	2.484E-06	395.1	2	1250	19.8	180	2.405E-06	3.17%	195
7	2.273E-06	339.9	2	1500	18.6	180	2.212E-06	2.70%	275
8	2.194E-06	298.4	2	1750	17.7	180	2.058E-06	6.17%	251
9	2.008E-06	265.3	2	2000	16.8	180	1.929E-06	3.93%	181
10	2.350E-06	247.0	2	2250	16.6	180	2.218E-06	5.63%	275
11	2.014E-06	232.9	2	2500	16.5	180	1.876E-06	6.83%	199
12	2.202E-06	221.3	2	2750	16.4	180	2.100E-06	4.63%	238
13	2.207E-06	211.0	2	3000	16.3	180	2.061E-06	6.63%	300
14	2.325E-06	184.0	2	3500	15.4	180	2.157E-06	7.23%	310
15	2.202E-06	179.3	2	4000	16.0	180	2.024E-06	8.11%	273
16	2.219E-06	170.0	2	4500	16.1	180	2.071E-06	6.67%	307
17	2.344E-06	157.4	2	5000	15.7	180	2.198E-06	6.21%	301
18	2.452E-06	574.7	5	40	8.1	180	2.390E-06	2.52%	33
19	2.408E-06	601.7	10	40	12.0	180	2.337E-06	2.96%	55
20	2.158E-06	495.7	20	40	14.0	180	2.128E-06	1.40%	67
21	2.365E-06	569.2	20	40	16.1	180	2.329E-06	1.54%	79
22	2.307E-06	586.8	40	40	23.5	180	2.247E-06	2.63%	143
23	2.291E-06	560.2	60	40	27.4	180	2.180E-06	4.84%	177
24	2.374E-06	545.3	80	40	30.8	180	2.234E-06	5.86%	207
25	2.290E-06	533.2	100	40	33.7	180	2.116E-06	7.58%	266
26	2.403E-06	556.2	120	40	38.5	180	2.246E-06	6.51%	357
27	2.335E-06	543.5	140	40	40.7	180	2.183E-06	6.49%	402
28	2.274E-06	537.2	160	40	43.0	180	2.133E-06	6.17%	510

3.2.2. NiTi Infrared Thermal Imaging

As previously mentioned, this EPT generally resulted in lower temperatures than what has been performed in previous studies [213,255,257,258]. Figure 3-6 and Figure 3-7 showcase IR images of NiTi sample 15 and NiTi sample 25, respectively, during EPT. NiTi sample 15 reached a maximum temperature of 272.7 °C, while NiTi sample 25 reached a maximum temperature of 265.8 °C.

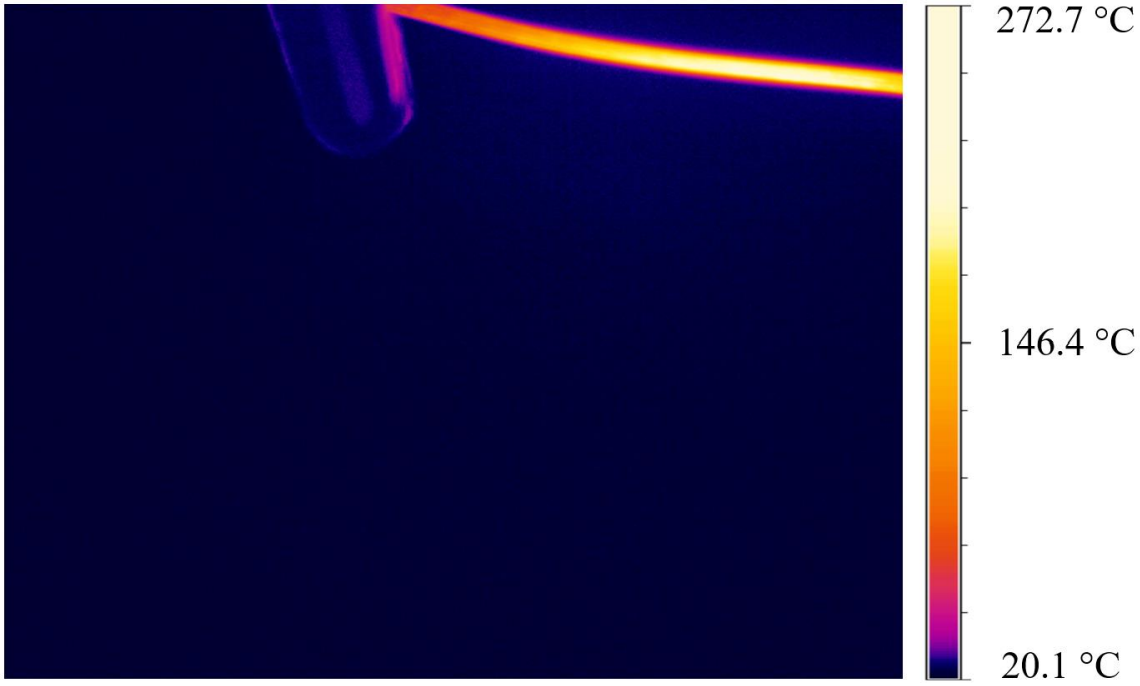

Figure **3-6**: Infrared thermal image of NiTi sample 15 during electropulsing treatment that resulted in a maximum temperature of 272.7 °C and resistivity reduction of 8.11%.

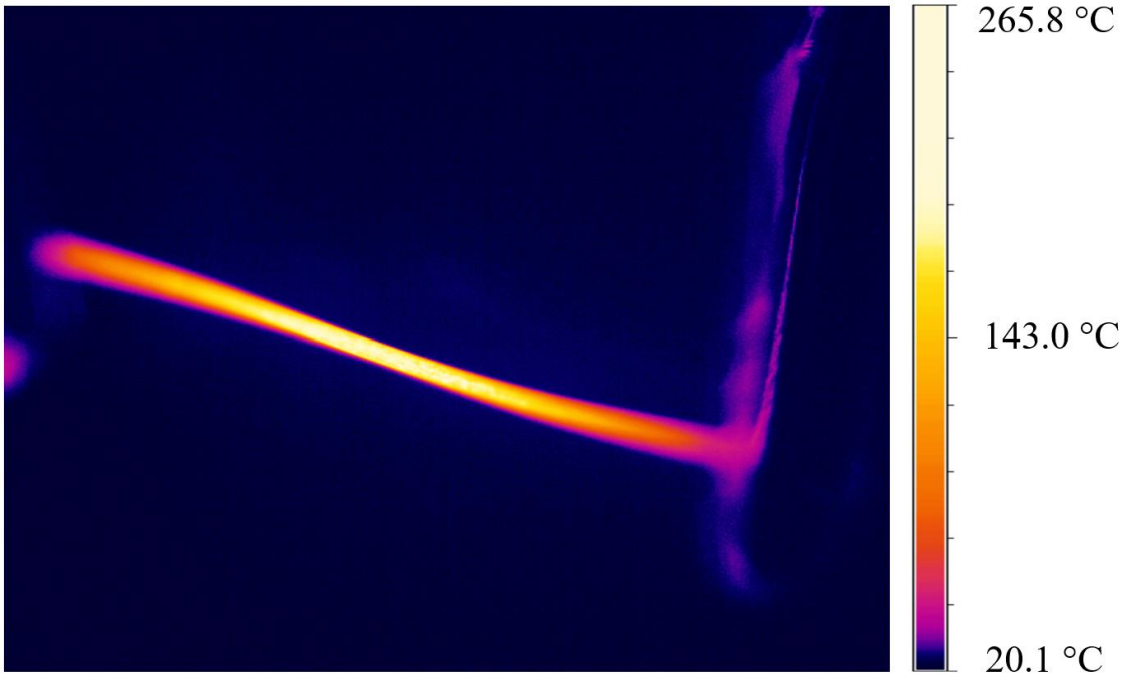

Figure **3-7**: Infrared thermal image of NiTi sample 25 during electropulsing treatment that resulted in a maximum temperature of 265.8 °C and resistivity reduction of 7.58%.

Chapter 4

Discussion

The following sections will discuss the results of EPT on $Ti_3C_2T_x$ MXene and NiTi SMA, respectively.

4.1. $Ti_3C_2T_x$ MXene

The following subsections will discuss the results of EPT on $Ti_3C_2T_x$ MXene through electrical resistivity reduction, IR thermal imaging, Raman spectroscopy, and FIB SEM.

4.1.1 $Ti_3C_2T_x$ Electrical Resistivity

As determined from the resistivity results, the EWF annealing process consisting of EPT and compressive loading does not provide a completely permanent change in resistivity for $Ti_3C_2T_x$ samples. The increase in resistivity after the immediate resistivity measurement varies largely, but appears to be less for the $Ti_3C_2T_x$ samples that displayed a larger initial resistivity reduction, such as $Ti_3C_2T_x$ samples C1 and C2. When measured immediately after EWF annealing, $Ti_3C_2T_x$ sample C1 had a resistivity reduction of 96.65%, which reduced to 94.80% when measured > 24 hours later. Similarly, $Ti_3C_2T_x$ sample C2 had an initial reduction of 95.58% and a reduction of 94.00% when measured > 24 hours later. The resistivity increase measured > 24 hours after EWF annealing was very small for these samples (1.58%–1.85%). On the other hand, the increase in resistivity > 24 hours later was significantly larger for $Ti_3C_2T_x$ samples C4–C6 (6.75%–22.00%). Although the time-dependence of this EWF annealing process is not

completely understood, the primary variables involved are believed to be the peak current density and amount of compressive loading that are used during the process.

The EWF annealing consisting of exclusively EPT resulted in a maximum resistivity reduction of 77.96%, displayed by $Ti_3C_2T_x$ sample E1. This reduction is comparable to the 2021 study in which a 72% resistivity reduction was achieved by EWF annealing $Ti_3C_2T_x$ MXene films with DC and current densities of 377 A/mm^2 [210]. The combination of this 2021 study and the present study suggests that a limit on the resistivity reduction exists for $Ti_3C_2T_x$ MXene through purely electrical or EWF annealing. This limit appears to be in the range of 72–78% resistivity reduction. These resistivity reductions are possible through heat treatment, but must be performed in inert or non-oxidative environments.

4.1.2. $Ti_3C_2T_x$ Infrared Thermal Imaging

IR thermal imaging shows that the maximum temperature during EWF annealing reached 30.7 °C, and that the process can be completed at RT. These temperatures are significantly below any temperatures previously used to anneal $Ti_3C_2T_x$. Contrasting $Ti_3C_2T_x$ samples E1 and E2 with the $Ti_3C_2T_x$ samples annealed via DC in the previously mentioned 2021 study, the resulting resistivity reduction was 72%, while the maximum temperature recorded was 120 °C [210]. As previously mentioned, $Ti_3C_2T_x$ and other titanium carbide MXenes oxidize in higher-temperature environments when in the presence of oxygen. For this reason, temperature should be minimized during EWF annealing processes in ambient conditions.

4.1.3. $Ti_3C_2T_x$ Raman Spectroscopy

Raman spectra show no changes in the composition of $Ti_3C_2T_x$, but a slight increase in T_x concentration after EWF annealing. Considering this is a RT annealing process, changes in composition or a reduction in surface terminations were not expected, as these have only been shown at very elevated temperatures. The slight increase in T_x concentration can likely be explained by the 1 month time difference between EWF annealing and Raman spectroscopy, considering $Ti_3C_2T_x$ is known to oxidize. The Raman spectra verify that the reduction in electrical resistivity is not coming from a reduction in surface terminations.

4.1.4. $Ti_3C_2T_x$ Focused Ion Beam Scanning Electron Microscopy

FIB SEM and ImageJ analysis show that there is a reduction in internal pore size after EWF annealing. EPT alone has been shown to heal cracks or voids in numerous metallic materials, including medium carbon steel [77], TC4 titanium [37], aluminum alloys [113], austenitic stainless steel [50,145], and SUS304 stainless steel [59]. As the current detours around the cracks in these materials, the cracks are healed from the crack tip [37,113]. Multiple applications of EPT have been shown to completely close cracks, with the cracks decreasing in size after each subsequent application of EPT [59,145]. However, Joule heating was present in all of these studies, and was hypothesized to be a prime contributor for crack healing, along with the current detour effect [59]. Because the average pore size was shown to decrease from this EWF annealing process performed at RT, Joule heating cannot be attributed to the pore healing. The magnitude of current density and the current detour effect are likely the prime contributing factors to pore healing in this process.

4.2. NiTi Shape Memory Alloy

The following subsection will discuss the results of EPT on NiTi SMA through electrical resistivity reduction and IR thermal imaging.

4.2.1. NiTi Electrical Resistivity

The maximum reduction in resistivity for NiTi samples was 8.11% after EPT. It is interesting to note that the largest resistivity reductions did not occur for the largest peak or RMS current densities, even though current density is typically thought of as the prime parameter for EPT. Furthermore, it is also interesting to note that a similar resistivity reduction was achieved for both NiTi samples 15 and 25 with significantly different electropulsing parameters. NiTi sample 15 displayed an 8.11% resistivity reduction after EPT with a peak current density of 179.3 A/mm^2, frequency of 2 Hz, and pulse width of 4000 µs. On the other hand, NiTi sample 25 displayed a similar reduction of 7.58% with a peak current density of 533.2 A/ mm^2, frequency of 100 Hz, and pulse width of 40 µs. Similar to the EPT of $Ti_3C_2T_x$ MXene, this suggests that there may be a limit to the resistivity reduction that can be achieved by EPT, given the specific experimental setup and high-transformation-temperature NiTi wire described previously.

4.2.2. NiTi Infrared Thermal Imaging

The sample with the largest resistivity reduction of 8.11%, NiTi sample 15, reached nearly 273 °C, while NiTi sample 25 reached nearly 266 °C. Other studies investigating EPT of NiTi have reported a maximum resistivity reduction of 11.2% while temperatures reached approximately 680 °C [255], as well as a maximum resistivity reduction of approximately 19.8% while temperatures reached approximately 325 °C [213,258]. A > 8% reduction in resistivity has

yet to be reported for NiTi undergoing EPT with resulting temperatures < 325 °C. Annealing NiTi through EPT at low-temperatures may be beneficial for material properties, especially for shape memory properties. Post-process HT or EPT will inevitably change the transformation temperature of NiTi alloys, which may not be desirable, depending upon the end-use application. Low-temperature post-processing through EPT will lead to a smaller change from the original transformation temperature, which may beneficial in these specific scenarios.

Chapter 5

Conclusion

This study investigating EPT of $Ti_3C_2T_x$ MXene and NiTi SMA showcases how effective electropulsing is in eliciting microstructural changes, and therefore, enhancing material properties. EPT is an effective alternative to traditional HT, and may be even more effective than traditional HT for certain materials, such as $Ti_3C_2T_x$ MXene, that oxidizes at elevated temperatures when in the presence of oxygen. Furthermore, EPT can be completed in significantly less time while utilizing less energy than traditional HT.

5.1. $Ti_3C_2T_x$ MXene

The EWF annealing of $Ti_3C_2T_x$ MXene results in a few key conclusions. First, EWF annealing with EPT and compressive loading can achieve a > 90% reduction in electrical resistivity for $Ti_3C_2T_x$ MXene. This > 90% reduction could likely be further improved by optimizing both EPT and compressive parameters. As showcased through research in crack healing with EPT [59,145], multiple applications may further reduce resistivity by healing internal pores. Most of this resistivity change is permanent, but more research must be performed to determine the exact permanence, as well as how to improve permanence of the process.

Second, EWF annealing with exclusively EPT can achieve > 75% reduction in electrical resistivity. This result, along with the 2021 study results [210], indicate that there is likely a limit to the resistivity reduction achieved by purely electrical current annealing. This limit appears to be in the range of 72–78% resistivity reduction. Both EWF annealing processes can be completed at RT and in ambient conditions.

Third, the resistivity reductions are primarily achieved by a reduction in average internal pore size. Internal porosity analysis of FIB SEM cross-sectional images performed in ImageJ shows a reduction in both average pore size and porosity volume fraction, with the most significant change being a reduction in pore size. After EWF annealing, the frequency of pore sizes < 600 nm^2 increased from 26.1% up to 30.1–38.8%. The frequency of nearly all other pore sizes decreased after EWF annealing. The reduction in pore size can likely be contributed to the magnitude of current density and the current detour effect.

Lastly, Raman spectra show no changes in composition of $Ti_3C_2T_x$, but a slight increase in T_x concentration after EWF annealing. Changes in composition through a reduction in surface terminations were not expected, due to the drastically low temperatures of EWF annealing. The slight increase in T_x concentration can be explained by the 1 month time difference between EWF annealing and Raman spectroscopy, considering $Ti_3C_2T_x$ is known to oxidize.

5.2. NiTi Shape Memory Alloy

Optimizing the EPT of high-transformation-temperature NiTi wire resulted in an electrical resistivity reduction > 8%. The largest resistivity reduction was a result of EPT with a peak current density of 179.3 A/mm^2, frequency of 2 Hz, and pulse width of 4000 μs, resulting in an RMS current density of 16.0 A/mm^2. Although this result was achieved with a low frequency and high pulse width, a similar resistivity reduction of 7.58% was achieved with a high frequency of 100 Hz and a low pulse width of 40 μs. These results indicate that there may be a limit on the resistivity reduction that can be achieved for the specific experimental setup and NiTi wire utilized. The temperatures of these NiTi samples reached 272.7 °C and 265.8 °C, respectively. EPT of NiTi with significant resistivity reductions and resulting temperatures < 325 °C have not been reported in previous studies.

References

[1] Källén, M., 2012, “Energy Efficiency Opportunities within the Heat Treatment Industry.”

[2] 2019, “Use of Energy Explained: Energy Use in Homes” [Online]. Available: https://www.eia.gov/energyexplained/use-of-energy/electricity-use-in-homes.php#:~:text=The average U.S. household consumes,kilowatthours (kWh) per year.&text=However%2C electricity use in homes,States and across housing types.

[3] Sheng, Y., Hua, Y., Wang, X., Zhao, X., Chen, L., Zhou, H., Wang, J., Berndt, C. C., and Li, W., 2018, “Application of High-Density Electropulsing to Improve the Performance of Metallic Materials: Mechanisms, Microstructure and Properties,” Materials (Basel)., **11**(2), pp. 1–25.

[4] Elliott-Bowman, B., 2016, “Electropulsing of Pearlitic Steels,” Imperial College London.

[5] Okazaki, K., Kagawa, M., and Conrad, H., 1980, “An Evaluation of the Contributions of Skin, Pinch and Heating Effects to the Electroplastic Effect in Titatnium,” Mater. Sci. Eng., **45**(2), pp. 109–116.

[6] Troitskii, O. A., 1985, “Pressure Shaping by the Application of a High Energy,” Mater. Sci. Eng., **75**(1–2), pp. 37–50.

[7] Conrad, H., 2000, “Electroplasticity in Metals and Ceramics,” Mater. Sci. Eng. A, **287**(2), pp. 276–287.

[8] Ho, P. S., and Kwok, T., 1989, “Electromigration in Metals,” Reports Prog. Phys., **52**(3), pp. 301–348.

[9] Misra, A. K., 1985, “A Novel Solidification Technique of Metals and Alloys: Under the Influence of Applied Potential,” Metall. Trans. A, **16**(7), pp. 1354–1355.

[10] Conrad, H., Karam, N., and Mannan, S., 1983, “Effect of Electric Current Pulses on the Recrystallization of Copper,” Scr. Metall., **17**, pp. 411–416.

[11] Conrad, H., Karam, N., and Mannan, S., 1984, “Effect of Prior Cold Work on the Influence of Electric Current Pulses on the Recrystallization of Copper,” Scr. Metall., **18**, pp. 275–280.

[12] Wang, X. L., Guo, J. D., Wang, Y. M., Wu, X. Y., and Wang, B. Q., 2006, “Segregation of Lead in Cu-Zn Alloy under Electric Current Pulses,” Appl. Phys. Lett., **89**(6), pp. 1–4.

[13] Xu, Z., Tang, G., Tian, S., and He, J., 2006, “Research on the Engineering Application of Multiple Pulses Treatment for Recrystallization of Fine Copper Wire,” Mater. Sci. Eng. A, **424**(1–2), pp. 300–306.

[14] Zhu, R. F., Liu, J. N., Tang, G. Y., Shi, S. Q., and Fu, M. W., 2012, "Properties, Microstructure and Texture Evolution of Cold Rolled Cu Strips under Electropulsing Treatment," J. Alloys Compd., **544**, pp. 203–208.

[15] Zhu, R. F., Tang, G. Y., Shi, S. Q., and Fu, M. W., 2013, "Microstructure Evolution of Copper Strips with Gradient Temperature in Electropulsing Treatment," J. Alloys Compd., **581**, pp. 160–165.

[16] Yin, Y., Chen, H., Morita, Y., Toku, Y., and Ju, Y., 2018, "Effect of Electropulsing Treatment on the Fatigue Crack Growth Behavior of Copper," Materials (Basel)., **11**(11).

[17] Rojas, H. A. G., Egea, A. J. S., Hameed, S., and Bolmaro, R., 2019, "An Ultra-Fast Annealing Treatment by Electropulsing during Pure Copper Wire Drawing," Metals (Basel)., **9**(12), pp. 1–10.

[18] Zhu, J., Liu, S., Lin, Y., and Wang, G., 2020, "Effect of Electropulsing on Microstructure and Properties of Severely Plastically Deformed Pure Copper Sheet," J. Mater. Eng. Perform., **29**(2), pp. 841–848.

[19] Conrad, H., Karam, N., Mannan, S., and Sprecher, A. F., 1988, "Effect of Electric Current Pulses on the Recrystallization Kinetics of Copper," Scr. Metall., **22**(2), pp. 235–238.

[20] Conrad, H., White, J., Cao, W. D., Lu, X. P., and Sprecher, A. F., 1991, "Effect of Electric Current Pulses on Fatigue Characteristics of Polycrystalline Copper," Mater. Sci. Eng. A, **145**(1), pp. 1–12.

[21] Xiao, S. H., Guo, J. D., Wu, S. D., He, G. H., and Li, S. X., 2002, "Recrystallization in Fatigued Copper Single Crystals under Electropulsing," Scr. Mater., **46**(1), pp. 1–6.

[22] Zhou, Y., Guo, J., Zhang, W., and He, G., 2002, "Influence of Electropulsing on Nucleation during Phase Transformation," J. Mater. Res., **17**(12), pp. 3012–3014.

[23] Valeev, I. S., and Kamalov, Z. G., 2003, "Structure Evolution in Copper Resulting from the Effect of Powerful Current Pulses," J. Mater. Eng. Perform., **12**(3), pp. 272–278.

[24] Zhou, Y., Zhang, W., Wang, B., and Guo, J., 2003, "Ultrafine-Grained Microstructure in a Cu-Zn Alloy Produced by Electropulsing Treatment," J. Mater. Res., **18**(8), pp. 1991–1997.

[25] Zhou, Y. Z., Zhang, W., Guo, J., and He, G., 2004, "Diffusive Phase Transformation in a Cu-Zn Alloy under Rapid Heating by Electropulsing," Philos. Mag. Lett., **84**(5), pp. 341–348.

[26] Zhou, Y., Xiao, S., and Guo, J., 2004, "Recrystallized Microstructure in Cold Worked Brass Produced by Electropulsing Treatment," Mater. Lett., **58**(12–13), pp. 1948–1951.

[27] Xu, Z. S., Lai, Z. H., and Chen, Y. X., 1988, "Effect of Electric Current on the Recrystallization Behavior of Cold Worked α - Ti," Scr. Metall., **22**(2), pp. 187–190.

[28] Zhang, W., Sui, M. L., Zhao, W. S., and Li, D. X., 2003, "Electropulsing-Induced Phase

Transformation in Titanium Alloy," Microsc. Microanal., **9**(SUPPL. 2), pp. 624–625.

[29] Ao, D. W., Chu, X. R., Lin, S. X., Yang, Y., and Gao, J., 2018, "Hot Tensile Behaviors and Microstructure Evolution of Ti-6Al-4V Titanium Alloy Under Electropulsing," Acta Metall. Sin. (English Lett., **31**(12), pp. 1287–1296.

[30] Zhao, Y., Shi, Y., Yang, X., and Xu, X., 2018, "Rapid Strengthening Without Loss of Ductility via Electropulsing Treatment in Ti-6Al-4V Alloy," J. Mater. Eng. Perform., **27**(7), pp. 3636–3642.

[31] Huang, J., Xu, Z., Deng, Y., and Peng, L., 2019, "Electropulsing-Induced α to β Phase Transformation of Ti-6Al-4V," J. Manuf. Sci. Eng. Trans. ASME, **141**(10).

[32] Gao, J. B., Ben, D. D., Yang, H. J., Meng, L. X., Ji, H. B., Lian, D. L., Chen, J., Yi, J. L., Wang, L., Li, P., and Zhang, Z. F., 2021, "Effects of Electropulsing on the Microstructure and Microhardness of a Selective Laser Melted Ti6Al4V Alloy," J. Alloys Compd., **875**.

[33] Shao, H., Zhang, H., Shan, D., Zhang, S., Wang, K., Sun, F., Fan, D., Wang, L., Zhuo, L., and Zou, J., 2021, "Evolution Behavior of Abnormal β Grain Region in Ti-5Al-5Mo-5V-1Cr-1Fe Titanium Alloy under the Electropulsing Treatment," Mater. Charact., **181**(June), p. 111504.

[34] Zhao, S., Zhang, R., Chong, Y., Li, X., Abu-Odeh, A., Rothchild, E., Chrzan, D. C., Asta, M., Morris, J. W., and Minor, A. M., 2021, "Defect Reconfiguration in a Ti–Al Alloy via Electroplasticity," Nat. Mater., **20**(4), pp. 468–472.

[35] Zhang, W., Zhao, W. S., Li, D. X., and Sui, M. L., 2004, "Martensitic Transformation from α-Ti to β-Ti on Rapid Heating," Appl. Phys. Lett., **84**(24), pp. 4872–4874.

[36] Song, H., Wang, Z.-J., and Gao, T.-J., 2007, "Effect of High Density Electropulsing Treatment on Formability of TC4 Titanium Alloy Sheet," Trans. Nonferrous Met. Soc. China, **17**(1), pp. 87–92.

[37] Song, H., and Wang, Z. J., 2008, "Microcrack Healing and Local Recrystallization in Pre-Deformed Sheet by High Density Electropulsing," Mater. Sci. Eng. A, **490**(1–2), pp. 1–6.

[38] Wang, Z. jin, and Song, H., 2009, "Effect of High-Density Electropulsing on Microstructure and Mechanical Properties of Cold-Rolled TA15 Titanium Alloy Sheet," J. Alloys Compd., **470**(1–2), pp. 522–530.

[39] Song, H., and Wang, Z.-J., 2012, "Improvement of Mechanical Properties of Cold-Rolled Commercially Pure Ti Sheet by High Density Electropulsing," Trans. Nonferrous Met. Soc. China, **22**(6), pp. 1350–1355.

[40] Song, H., Wang, Z.-J., and He, X.-D., 2013, "Improving in Plasticity of Orthorhombic Ti2AlNb-Based Alloys Sheet by High Density Electropulsing," Trans. Nonferrous Met. Soc. China, **23**(1), pp. 32–37.

[41] Zhou, Y., Chen, G., Fu, X.-S., and Zhou, W.-L., 2014, "Effect of Electropulsing on Deformation Behavior of Ti-6Al-4V Alloy during Cold Drawing," Trans. Nonferrous Met.

Soc. China, **24**(4), pp. 1012–1021.

[42] Ye, X., Yang, Y., Song, G., and Tang, G., 2014, "Enhancement of Ductility, Weakening of Anisotropy Behavior and Local Recrystallization in Cold-Rolled Ti-6Al-4V Alloy Strips by High-Density Electropulsing Treatment," Appl. Phys. A Mater. Sci. Process., **117**(4), pp. 2251–2264.

[43] Lai, Z. H., Conrad, H., Chao, Y. S., Wang, S. Q., and Sun, J., 1989, "Effect of Electropulsing on the Microstructure and Properties of Iron-Based Amorphous Alloys," Scr. Metall., **23**(3), pp. 305–310.

[44] Lai, Z. H., Chao, Y. S., Conrad, H., and Chu, K., 1995, "Hyperfine-Structure Changes in Iron-Base Amorphous-Alloys Produced by High-Current Density Electropulsing," J. Mater. Res., **10**(4), pp. 900–906.

[45] Teng, G. Q., Chao, Y. S., Lai, Z. H., and dong, L., 1995, "Rapid Nanocrystallization from Amorphous Fe78B13Si9 by High Current Density Electropulsing," J. Mater. Sci. Lett., **14**(2), pp. 144–145.

[46] Gao, M., Liu, H., Xu, B., Liu, W., and Li, Q., 2019, "Reverse Evolution in Nanoscale Cu-Rich Precipitates of an Aged Fe–Cu Alloy under Electropulsing," Philos. Mag. Lett., **99**(1), pp. 39–47.

[47] Zhou, Y., Qin, R., Xiao, S., He, G., and Zhou, B., 2000, "Reversing Effect of Electropulsing on Damage of 1045 Steel," J. Mater. Res., **15**(5), pp. 1056–1061.

[48] Ma, B., Zhao, Y., Ma, J., Guo, H., and Yang, Q., 2013, "Formation of Local Nanocrystalline Structure in a Boron Steel Induced by Electropulsing," J. Alloys Compd., **549**, pp. 77–81.

[49] Zhang, X. F., Lu, W. J., and Qin, R. S., 2013, "Removal of MnS Inclusions in Molten Steel Using Electropulsing," Scr. Mater., **69**(6), pp. 453–456.

[50] Hosoi, A., Kishi, T., and Ju, Y., 2013, "Healing of Fatigue Crack by High-Density Electropulsing in Austenitic Stainless Steel Treated with the Surface-Activated Pre-Coating," Materials (Basel)., **6**(9), pp. 4213–4225.

[51] Tang, Y., Hosoi, A., Morita, Y., and Ju, Y., 2013, "Restoration of Fatigue Damage in Stainless Steel by High-Density Electric Current," Int. J. Fatigue, **56**, pp. 69–74.

[52] Lu, W. J., Zhang, X. F., and Qin, R. S., 2014, "Electropulsing-Induced Strengthening of Steel at High Temperature," Philos. Mag. Lett., **94**(11), pp. 688–695.

[53] Lu, W. J., Zhang, X. F., and Qin, R. S., 2015, "Stability of Precipitates under Electropulsing in 316L Stainless Steel," Mater. Sci. Technol. (United Kingdom), **31**(13a), pp. 1530–1535.

[54] Wang, H., Song, G., and Tang, G., 2015, "Enhanced Surface Properties of Austenitic Stainless Steel by Electropulsing-Assisted Ultrasonic Surface Rolling Process," Surf. Coatings Technol., **282**, pp. 149–154.

[55] Rahnama, A., and Qin, R. S., 2015, "The Effect of Electropulsing on the Interlamellar Spacing and Mechanical Properties of a Hot-Rolled 0.14% Carbon Steel," Mater. Sci. Eng. A, **627**, pp. 145–152.

[56] Lu, W. J., and Qin, R. S., 2016, "Influence of κ-Carbide Interface Structure on the Formability of Lightweight Steels," Mater. Des., **104**, pp. 211–216.

[57] Lu, W. J., and Qin, R. S., 2016, "Stability of Martensite with Pulsed Electric Current in Dual-Phase Steels," Mater. Sci. Eng. A, **677**, pp. 252–258.

[58] Zhou, Y., Zhang, W., Wang, B., He, G., and Guo, J., 2002, "Grain Refinement and Formation of Ultrafine-Grained Microstructure in a Low-Carbon Steel under Electropulsing," J. Mater. Res., **17**(8), pp. 2105–2111.

[59] Yu, T., Deng, D., Wang, G., and Zhang, H., 2016, "Crack Healing in SUS304 Stainless Steel by Electropulsing Treatment," J. Clean. Prod., **113**, pp. 989–994.

[60] Pan, L., He, W., and Gu, B., 2016, "Effects of Electric Current Pulses on Mechanical Properties and Microstructures of As-Quenched Medium Carbon Steel," Mater. Sci. Eng. A, **662**, pp. 404–411.

[61] Rahnama, A., and Qin, R., 2017, "Room Temperature Texturing of Austenite/Ferrite Steel by Electropulsing," Sci. Rep., **7**, pp. 1–6.

[62] Lesiuk, G., Zimniak, Z., Wiśniewski, W., and Correia, J. A. F. O., 2017, "Fatigue Lifetime Improvement in AISI 304 Stainless Steel Due to High-Density Electropulsing," Procedia Struct. Integr., **5**, pp. 928–934.

[63] Yang, C. L., Yang, H. J., Zhang, Z. J., and Zhang, Z. F., 2018, "Recovery of Tensile Properties of Twinning-Induced Plasticity Steel via Electropulsing Induced Void Healing," Scr. Mater., **147**, pp. 88–92.

[64] Ben, D. D., Yang, H. J., Ma, Y. R., Shao, X. H., Pang, J. C., and Zhang, Z. F., 2018, "Rapid Hardening of AISI 4340 Steel Induced by Electropulsing Treatment," Mater. Sci. Eng. A, **725**(January), pp. 28–32.

[65] Ma, Y. R., Yang, H. J., Tian, Y. Z., Pang, J. C., and Zhang, Z. F., 2018, "Hardening and Softening Mechanisms in a Nano-Lamellar Austenitic Steel Induced by Electropulsing Treatment," Mater. Sci. Eng. A, **713**(July 2017), pp. 146–150.

[66] Ben, D., Yang, H., Ma, Y., Wang, Q., Tian, Y., Zhang, P., Duan, Q., and Zhang, Z., 2019, "Declined Fatigue Crack Propagation Rate of a High-Strength Steel by Electropulsing Treatment," Adv. Eng. Mater., **21**(7), pp. 1–8.

[67] Wang, F., Qian, D., Hua, L., Mao, H., and Xie, L., 2019, "Voids Healing and Carbide Refinement of Cold Rolled M50 Bearing Steel by Electropulsing Treatment," Sci. Rep., **9**(1), pp. 1–7.

[68] Xiang, S., and Zhang, X., 2020, "Residual Stress Removal Under Pulsed Electric Current," Acta Metall. Sin. (English Lett., **33**(2), pp. 281–289.

[69] Zhou, Y., Zhang, W., Sui, M., Li, D., He, G., and Guo, J., 2002, "Formation of a Nanostructure in a Low-Carbon Steel under High Current Density Electropulsing," J. Mater. Res., **17**(5), pp. 921–924.

[70] Qin, S., Ba, X., and Zhang, X., 2020, "Accelerated Cluster Dissolution Using Electropulsing for Ultrafast Performance Regeneration," Scr. Mater., **178**, pp. 24–28.

[71] Noell, P. J., Rodelas, J. M., Ghanbari, Z. N., and Laursen, C. M., 2020, "Microstructural Modification of Additively Manufactured Metals by Electropulsing," Addit. Manuf., **33**(February).

[72] Zeng, Z., He, J., Xiang, Z., Sun, Q., Wu, Y., and Wang, S., 2020, "Embrittlement of 316L Stainless Steel in Electropulsing Treatment," J. Mater. Res. Technol., **9**(5), pp. 10669–10678.

[73] Ding, S., Xiang, S., Ba, X., Zhang, X., and Fu, Y., 2020, "Improvement of Corrosion Resistance of Simulated Weld Heat Affected Zone in High Strength Pipeline Steel Using Electropulsing," ISIJ Int., **60**(9), pp. 2015–2023.

[74] Hao, J., Zhang, H., Zhang, X., and Liu, C., 2020, "Accelerated Carbon Atoms Diffusion in Bearing Steel Using Electropulsing to Reduce Spheroidization Processing Time and Improve Microstructure Uniformity," Steel Res. Int., **91**(7), pp. 1–11.

[75] Agrawal, M., Bhuyan, D., Pandey, R. K., Sharma, A., and Manna, R., 2021, "Effect of Electropulsing on Nanostructured Bainitic Steel," J. Mater. Eng. Perform.

[76] Duan, C., Qu, S., Hu, X., Jia, S., and Li, X., 2022, "Microstructures and Fatigue Behaviors of 25CrNi2MoV Steel under Electropulsing-Assisted Ultrasonic Surface Rolling," Int. J. Fatigue, **158**(November 2021), p. 106733.

[77] Zhou, Y., Guo, J., Gao, M., and He, G., 2004, "Crack Healing in a Steel by Using Electropulsing Technique," Mater. Lett., **58**(11), pp. 1732–1736.

[78] Samuel, E. I., Bhowmik, A., and Qin, R., 2010, "Accelerated Spheroidization Induced by High Intensity Electric Pulse In a Severely Deformed Eutectold Steel," J. Mater. Res., **25**(6), pp. 1020–1024.

[79] Konovalov, S. V., Atroshkina, A. A., Ivanov, Y. F., and Gromov, V. E., 2010, "Evolution of Dislocation Substructures in Fatigue Loaded and Failed Stainless Steel with the Intermediate Electropulsing Treatment," Mater. Sci. Eng. A, **527**(12), pp. 3040–3043.

[80] Qin, R. S., Samuel, E. I., and Bhowmik, A., 2011, "Electropulse-Induced Cementite Nanoparticle Formation in Deformed Pearlitic Steels," J. Mater. Sci., **46**(9), pp. 2838–2842.

[81] Hu, G., Zhu, Y., Tang, G., Shek, C., and Liu, J., 2011, "Effect of Electropulsing on Recrystallization and Mechanical Properties of Silicon Steel Strips," J. Mater. Sci. Technol., **27**(11), pp. 1034–1038.

[82] Dai, W., Wang, X., Zhao, H., and Zhao, X., 2012, "Effect of Electric Current on

Microstructural Evolution in a Cold-Rolled 3% Si Steel," Mater. Trans., **53**(1), pp. 229–233.

[83] Chu, X. R., Lin, S. X., Yue, Z. M., Gao, J., and Zhang, C. S., 2015, "Research of Initial Dynamic Recrystallisation for AZ31 Alloy with Pulse Current," Mater. Sci. Technol. (United Kingdom), **31**(13a), pp. 1601–1606.

[84] Xu, Z., Tang, G., Ding, F., Tian, S., and Tian, H., 2007, "The Effect of Multiple Pulse Treatment on the Recrystallization Behavior of Mg-3Al-1Zn Alloy Strip," Appl. Phys. A Mater. Sci. Process., **88**(2), pp. 429–433.

[85] Guan, L., Tang, G., Jiang, Y., and Chu, P. K., 2009, "Texture Evolution in Cold-Rolled AZ31 Magnesium Alloy during Electropulsing Treatment," J. Alloys Compd., **487**(1–2), pp. 309–313.

[86] Jiang, Y., Tang, G., Shek, C., Xie, J., Xu, Z., and Zhang, Z., 2012, "Mechanism of Electropulsing Induced Recrystallization in a Cold-Rolled Mg-9Al-1Zn Alloy," J. Alloys Compd., **536**, pp. 94–105.

[87] Zhang, D., To, S., Zhu, Y. H., Wang, H., and Tang, G. Y., 2012, "Static Electropulsing-Induced Microstructural Changes and Their Effect on the Ultra-Precision Machining of Cold-Rolled AZ91 Alloy," Metall. Mater. Trans. A Phys. Metall. Mater. Sci., **43**(4), pp. 1341–1346.

[88] Zhang, D., To, S., Zhu, Y. H., Wang, H., and Tang, G. Y., 2012, "Electropulsing-Induced Phase Transformations and Their Effects on the Single Point Diamond Turning of a Tempered Alloy AZ91," Int. J. Mater. Res., **103**(10), pp. 1205–1209.

[89] Zhang, D., To, S., Zhu, Y. H., Wang, H., and Tang, G. Y., 2012, "Dynamic Electropulsing-Induced Phase Transformations and Their Effects on the Single Point Diamond Turning of a Tempered Alloy AZ91," Int. J. Mater. Res., **103**(10), pp. 1205–1209.

[90] Li, C., Zhang, K. F., Jiang, S. S., and Zhao, Z. P., 2012, "Pulse Current Auxiliary Bulging and Deformation Mechanism of AZ31 Magnesium Alloy," Mater. Des., **34**, pp. 170–178.

[91] Xu, C., Li, Y., and Rao, X., 2014, "Effect of Electropulsing Rolling on Mechanical Properties and Microstructure of AZ31 Magnesium Alloy," Trans. Nonferrous Met. Soc. China, **24**(12), pp. 3777–3784.

[92] Cao, F., Xia, F., Hou, H., Ding, H., and Li, Z., 2015, "Effects of High-Density Pulse Current on Mechanical Properties and Microstructure in a Rolled Mg-9.3Li-1.79Al-1.61Zn Alloy," Mater. Sci. Eng. A, **637**, pp. 89–97.

[93] Jiang, Y., Guan, L., Tang, G., and Zhang, Z., 2015, "Improved Mechanical Properties of Mg-9Al-1Zn Alloy by the Combination of Aging, Cold-Rolling and Electropulsing Treatment," J. Alloys Compd., **626**, pp. 297–303.

[94] Liu, Y., Fan, J., Zhang, H., Jin, W., Dong, H., and Xu, B., 2015, "Recrystallization and Microstructure Evolution of the Rolled Mg-3Al-1Zn Alloy Strips under Electropulsing

Treatment," J. Alloys Compd., **622**, pp. 229–235.

[95] Bao, W., Chu, X., Lin, S., and Gao, J., 2015, "Experimental Investigation on Formability and Microstructure of AZ31B Alloy in Electropulse-Assisted Incremental Forming," Mater. Des., **87**, pp. 632–639.

[96] Guan, L., Tang, G., Chu, P. K., and Jiang, Y., 2009, "Enhancement of Ductility in Mg-3Al-1Zn Alloy with Tilted Basal Texture by Electropulsing," J. Mater. Res., **24**(12), pp. 3674–3679.

[97] Jin, W., Fan, J., Zhang, H., Liu, Y., Dong, H., and Xu, B., 2015, "Microstructure, Mechanical Properties and Static Recrystallization Behavior of the Rolled ZK60 Magnesium Alloy Sheets Processed by Electropulsing Treatment," J. Alloys Compd., **646**, pp. 1–9.

[98] Lin, S. X., Chu, X. R., Bao, W. K., Gao, J., and Ruan, L. Q., 2015, "Experimental Investigation of Pulse Current on Mechanical Behaviour of AZ31 Alloy," Mater. Sci. Technol. (United Kingdom), **31**(9), pp. 1131–1138.

[99] Wang, X., Xu, J., Shan, D., Guo, B., and Cao, J., 2016, "Modeling of Thermal and Mechanical Behavior of a Magnesium Alloy AZ31 during Electrically-Assisted Micro-Tension," Int. J. Plast., **85**, pp. 230–257.

[100] Jin, W., Fan, J., Zhang, H., Yang, L., Dong, H. B., and Xu, B., 2016, "Influence of Electropulsing Treatment on Microstructure Evolution and Properties of ZK60 Alloy Sheets," Rare Met. Meterials Eng., **46**(9), pp. 2965–2701.

[101] Zhu, X. X., Zhang, X. W., Wang, L. F., Chen, Z. Q., and Cao, X. Q., 2020, "The Effect of Electropulsing Treatment on Properties of Pre-Compressed AZ31 Magnesium Alloy," Mater. Res., **22**(6).

[102] Wang, X., Xu, C., Li, Y., and Wang, B., 2020, "Respective Roles of the Thermal and Electromigration Effect in AZ31 Mg Alloy during Low-Frequency Electropulsing Tension," J. Alloys Compd., **846**.

[103] Shan, Z., Yang, J., Fan, J., Zhang, H., Zhang, Q., Wu, Y., and Dong, H., 2020, "Microstructure Evolution and Mechanical Properties of an AZ61 Alloy Processed with TS-ECAP and EPT," Mater. Sci. Eng. A, **780**(December 2019), p. 139195.

[104] Jiang, B., Zhang, D., Xu, H., Liu, Y., Cao, Z., and Yang, X., 2021, "Excellent Ductility in the Extruded Az61 Magnesium Alloy Tube Induced by Electropulsing Treatment during Tension," Metals (Basel)., **11**(5).

[105] Zhang, G., Qin, S., Yan, L., and Zhang, X., 2021, "Superior Dehydrogenation Performance of Mg-Based Alloy under Electropulsing," Scr. Mater., **197**, p. 113788.

[106] Jiang, Y., Tang, G., Shek, C., and Zhu, Y., 2009, "Effect of Electropulsing Treatment on Microstructure and Tensile Fracture Behavior of Aged Mg-9Al-1Zn Alloy Strip," Appl. Phys. A Mater. Sci. Process., **97**(3), pp. 607–615.

[107] Jiang, Y., Tang, G., Shek, C., Zhu, Y., and Xu, Z., 2009, "On the Thermodynamics and Kinetics of Electropulsing Induced Dissolution of β-Mg17Al12 Phase in an Aged Mg-9Al-1Zn Alloy," Acta Mater., **57**(16), pp. 4797–4808.

[108] Xu, Q., Guan, L., Jiang, Y., Tang, G., and Wang, S., 2010, "Improved Plasticity of Mg-Al-Zn Alloy by Electropulsing Tension," Mater. Lett., **64**(9), pp. 1085–1087.

[109] Xu, Q., Tang, G., and Jiang, Y., 2011, "Thermal and Electromigration Effects of Electropulsing on Dynamic Recrystallization in Mg-3Al-1Zn Alloy," Mater. Sci. Eng. A, **528**(13–14), pp. 4431–4436.

[110] Xu, Q., Tang, G., Jiang, Y., Hu, G., and Zhu, Y., 2011, "Accumulation and Annihilation Effects of Electropulsing on Dynamic Recrystallization in Magnesium Alloy," Mater. Sci. Eng. A, **528**(7–8), pp. 3249–3252.

[111] Jiang, Y., Guan, L., Tang, G., Shek, C., and Zhang, Z., 2011, "Influence of Electropulsing Treatment on Microstructure and Mechanical Properties of Cold-Rolled Mg-9Al-1Zn Alloy Strip," Mater. Sci. Eng. A, **528**(16–17), pp. 5627–5635.

[112] Liao, H., Tang, G., Jiang, Y., Xu, Q., Sun, S., and Liu, J., 2011, "Effect of Thermo-Electropulsing Rolling on Mechanical Properties and Microstructure of AZ31 Magnesium Alloy," Mater. Sci. Eng. A, **529**(1), pp. 138–142.

[113] Qiao, S., Li, Y., Li, Y., and Zhang, C., 2009, "Damage Healing of Aluminum Alloys by D. C. Electropulsing and Evaluation by Resistance," Xiyou Jinshu Cailiao Yu Gongcheng/Rare Met. Mater. Eng., **38**(4), pp. 570–573.

[114] Zheng, Y. S., Tang, G. Y., Kuang, J., and Zheng, X. P., 2014, "Effect of Electropulse on Solid Solution Treatment of 6061 Aluminum Alloy," J. Alloys Compd., **615**, pp. 849–853.

[115] Xiao, H., Jiang, S., Zhang, K., Jia, Y., Shi, C., Lu, Z., and Jiang, J., 2020, "Optimizing the Microstructure and Mechanical Properties of a Cold-Rolled Al–Mg–Li Alloy via Electropulsing Assisted Recrystallization Annealing and Ageing," J. Alloys Compd., **814**, p. 152257.

[116] Chen, K., Zhan, L., and Yu, W., 2021, "Rapidly Modifying Microstructure and Mechanical Properties of AA7150 Al Alloy Processed with Electropulsing Treatment," J. Mater. Sci. Technol., **95**, pp. 172–179.

[117] Zhou, C., Zhan, L., and Li, H., 2021, "Improving Creep Age Formability of an Al-Cu-Li Alloy by Electropulsing," J. Alloys Compd., **870**.

[118] Xu, X., Zhao, Y., Ma, B., Zhang, J., and Zhang, M., 2014, "Rapid Grain Refinement of 2024 Al Alloy through Recrystallization Induced by Electropulsing," Mater. Sci. Eng. A, **612**, pp. 223–226.

[119] Xu, X., Zhao, Y., Ma, B., and Zhang, M., 2014, "Rapid Precipitation of T-Phase in the 2024 Aluminum Alloy via Cyclic Electropulsing Treatment," J. Alloys Compd., **610**, pp. 506–510.

[120] Xu, X., Zhao, Y., Ma, B., and Zhang, M., 2015, “Electropulsing Induced Evolution of Grain-Boundary Precipitates without Loss of Strength in the 7075 Al Alloy,” Mater. Charact., **105**, pp. 90–94.

[121] Xu, X., Zhao, Y., Wang, X., Zhang, Y., and Ning, Y., 2016, “Effect of Rapid Solid-Solution Induced by Electropulsing on the Microstructure and Mechanical Properties in 7075 Al Alloy,” Mater. Sci. Eng. A, **654**, pp. 278–281.

[122] Lu, Z., Guo, C., Li, P., Wang, Z., Chang, Y., Tang, G., and Jiang, F., 2017, “Effect of Electropulsing Treatment on Microstructure and Mechanical Properties of Intermetallic Al3Ti Alloy,” J. Alloys Compd., **708**, pp. 834–843.

[123] Yan, J., Li, W., Liu, H., and Shen, Y., 2019, “Reversion of Sub-Boundaries into Dense Dislocations in Aluminum by Electric Pulsing Treatment,” Scr. Mater., **167**, pp. 86–90.

[124] Xiao, H., Zhang, K., Shi, C., Lu, Z., and Jiang, J., 2019, “Influence of Electropulsing Treatment Combined with Pre-Deformation on Ageing Behavior and Mechanical Properties of 5A90 Al-Li Alloy,” J. Alloys Compd., **784**, pp. 1234–1247.

[125] Xiao, H., Jiang, S., Shi, C., Zhang, K., Lu, Z., and Jiang, J., 2019, “Study on the Microstructure Evolution and Mechanical Properties of an Al-Mg-Li Alloy Aged by Electropulsing Assisted Ageing Processing,” Mater. Sci. Eng. A, **756**(March), pp. 442–454.

[126] Zhu, Y. H., To, S., Lee, W. B., Liu, X. M., Jiang, Y. B., and Tang, G. Y., 2009, “Effects of Dynamic Electropulsing on Microstructure and Elongation of a Zn-Al Alloy,” Mater. Sci. Eng. A, **501**(1–2), pp. 125–132.

[127] Zhu, Y., To, S., Lee, W., Liu, X., Jiang, Y., and Tang, G., 2009, “Electropulsing-Induced Phase Transformations in a Zn-Al-Based Alloy,” J. Mater. Res., **24**(8), pp. 2661–2669.

[128] To, S., Zhu, Y. H., Lee, W. B., Liu, X. M., Jiang, Y. B., and Tang, G. Y., 2009, “Effects of Current Density on Electropulsing-Induced Phase Transformations in a Zn-Al Based Alloy,” Appl. Phys. A Mater. Sci. Process., **96**(4), pp. 939–944.

[129] To, S., Zhu, Y. H., Lee, W. B., Liu, X. M., and Jiang, Y. B., 2009, “Effects of Current Density on Elongation of an Electropulsing Treated Zn-Al Based Alloy,” Mater. Trans., **50**(12), pp. 2772–2777.

[130] To, S., Zhu, Y., W. B., L., and Liu, X. M., 2010, “Dynamic Electropulsing Induced Phase Transformations in a Furnace Cooled Zn-Al Based Alloy (ZA22),” Mater. Trans., **51**(11), pp. 1997–2004.

[131] Zhu, Y., To, S., Liu, X., and Hu, G., 2011, “Effect of Static Electropulsing on Microstructure and Elongation of a Zn-Al Alloy (ZA22),” Metall. Mater. Trans. A Phys. Metall. Mater. Sci., **42**(7), pp. 1933–1940.

[132] Zhu, Y. H., To, S., and Liu, X. M., 2011, “Use of EBSD to Study Electropulsing Induced Reverse Phase Transformations in a Zn-Al Alloy (ZA22),” J. Microsc., **242**(1), pp. 62–69.

[133] Zhu, Y. H., Jiang, S. Q., Zhao, D. D., Cheng, G. J., Zhang, H. W., and Lai, W. E., 2013, "Electropulsing Induced Crystal Orientation Change and Its Effects on Electric Conductivity of Nanofilms of Zn-Al Alloys," Appl. Phys. A Mater. Sci. Process., **111**(4), pp. 1241–1245.

[134] Zhu, Y. H., Jiang, Y. B., and Liu, X. M., 2018, "Electropulsing Induced Circular Phase Transformations of a Cold-Deformed ZA27 Alloy," J. Alloys Compd., **737**, pp. 630–636.

[135] Yuan, Y., Liu, W., Fu, B., Xu, H., Luo, G., Tang, G., and Jiang, Y., 2012, "The Effects of Electropulsing on the Recrystallization Behavior of Rolled Pure Tungsten," J. Mater. Res., **27**(20), pp. 2630–2638.

[136] Qin, R., and Su, S., 2002, "Thermodynamics of Crack Healing under Electropulsing," J. Mater. Res., **17**(8), pp. 2048–2052.

[137] Hosoi, A., Yano, T., Morita, Y., and Ju, Y., 2014, "Quantitative Evaluation of the Displacement Distribution and Stress Intensity Factor of Fatigue Cracks Healed by a Controlled High-Density Electric Current Field," Fatigue Fract. Eng. Mater. Struct., **37**(9), pp. 1025–1033.

[138] Waryoba, D., Islam, Z., Wang, B., and Haque, A., 2019, "Low Temperature Annealing of Metals with Electrical Wind Force Effects," J. Mater. Sci. Technol., **35**(4), pp. 465–472.

[139] Tskhondiya, G. A., and Beklemishev, N. N., 2012, "Simulating the Effect of a High Density Electric Current Pulse on the Stress Field during Plastic Deformation," Int. J. Mater. Form., **5**(2), pp. 157–162.

[140] Li, D., and Yu, E., 2009, "Computation Method of Metal's Flow Stress for Electroplastic Effect," Mater. Sci. Eng. A, **505**(1–2), pp. 62–64.

[141] Magargee, J., Morestin, F., and Cao, J., 2013, "Characterization of Flow Stress for Commercially Pure Titanium Subjected to Electrically Assisted Deformation," J. Eng. Mater. Technol. Trans. ASME, **135**(4), pp. 1–10.

[142] Xiao, S., Han, E., and Guo, J., 2006, "Effect of High Current Density Electropulsing on the Corrosion Resistance of X70 Pipeline Steel," Chinese J. Mater. Res., **20**(1), pp. 1–4.

[143] Bao, W., Chu, X., Lin, S., and Gao, J., 2017, "Electro-Plastic Effect on Tensile Deformation Behaviour and Microstructural Mechanism of AZ31B Alloy," Mater. Sci. Technol. (United Kingdom), **33**(7), pp. 836–845.

[144] Wang, S., Tang, G., Xu, Z., and Gaun, L., 2010, "High Energy Electric Pulse Treatment on Corrosion Performance of Magnesium Alloys," Rare Met. Meterials Eng., **39**(11), pp. 1997–2002.

[145] Hosoi, A., Nagahama, T., and Ju, Y., 2012, "Fatigue Crack Healing by a Controlled High Density Electric Current Field," Mater. Sci. Eng. A, **533**, pp. 38–42.

[146] Hao, T., Tanimoto, H., and Mizubayashi, H., 2005, "Transformation to Nanocrystallites in Amorphous Alloys Induced by Resonant Electropulsing," Mater. Trans., **46**(12), pp.

2898–2907.

[147] Naguib, M., Kurtoglu, M., Presser, V., Lu, J., Niu, J., Heon, M., Hultman, L., Gogotsi, Y., and Barsoum, M. W., 2011, "Two-Dimensional Nanocrystals Produced by Exfoliation of Ti3AlC2," Adv. Mater., **23**(37), pp. 4248–4253.

[148] Naguib, M., Mashtalir, O., Carle, J., Presser, V., Lu, J., Hultman, L., Gogotsi, Y., and Barsoum, M. W., 2012, "Two-Dimensional Transition Metal Carbides," ACS Nano, **6**(2), pp. 1322–1331.

[149] Kurtoglu, M., Naguib, M., Gogotsi, Y., and Barsoum, M. W., 2012, "First Principles Study of Two-Dimensional Early Transition Metal Carbides," MRS Commun., **2**(4), pp. 133–137.

[150] Xie, Y., Dall'Agnese, Y., Naguib, M., Gogotsi, Y., Barsoum, M. W., Zhuang, H. L., and Kent, P. R. C., 2014, "Prediction and Characterization of Mxene Nanosheet Anodes for Non-Lithium-Ion Batteries," ACS Nano, **8**(9), pp. 9606–9615.

[151] Rakhi, R. B., Ahmed, B., Hedhili, M. N., Anjum, D. H., and Alshareef, H. N., 2015, "Effect of Postetch Annealing Gas Composition on the Structural and Electrochemical Properties of Ti2CTx MXene Electrodes for Supercapacitor Applications," Chem. Mater., **27**(15), pp. 5314–5323.

[152] Xiong, D., Li, X., Bai, Z., and Lu, S., 2018, "Recent Advances in Layered Ti3C2Tx MXene for Electrochemical Energy Storage," Small, **14**(17), pp. 1–29.

[153] Anasori, B., and Gogotsi, Y., 2019, *2D Metal Carbides and Nitrides (MXenes)*.

[154] Gogotsi, Y., and Anasori, B., 2019, "The Rise of MXenes," ACS Nano, **13**(8), pp. 8491–8494.

[155] Zhang, Z., Yao, Z., Zhang, X., and Jiang, Z., 2020, "2D Carbide MXene under Postetch Low-Temperature Annealing for High–Performance Supercapacitor Electrode," Electrochim. Acta, **359**, p. 136960.

[156] Hong, W., Wyatt, B. C., Nemani, S. K., and Anasori, B., 2020, "Double Transition-Metal MXenes: Atomistic Design of Two-Dimensional Carbides and Nitrides," MRS Bull., **45**(10), pp. 850–861.

[157] Mathis, T. S., Maleski, K., Goad, A., Sarycheva, A., Anayee, M., Foucher, A. C., Hantanasirisakul, K., Shuck, C. E., Stach, E. A., and Gogotsi, Y., 2021, "Modified MAX Phase Synthesis for Environmentally Stable and Highly Conductive Ti3C2 MXene," ACS Nano, **15**(4), pp. 6420–6429.

[158] Xu, H., Yin, X., Li, X., Li, M., Zhang, L., and Cheng, L., 2019, "Thermal Stability and Dielectric Properties of 2D Ti2C MXenes via Annealing under a Gas Mixture of Ar and H2 Atmosphere," Funct. Compos. Struct., **1**(1).

[159] Wyatt, B. C., Nemani, S. K., Desai, K., Kaur, H., Zhang, B., and Anasori, B., 2021, "High-Temperature Stability and Phase Transformations of Titanium Carbide (Ti3C2Tx)

MXene," J. Phys. Condens. Matter, **33**(22).

[160] Lipatov, A., Lu, H., Alhabeb, M., Anasori, B., Gruverman, A., Gogotsi, Y., and Sinitskii, A., 2018, "Elastic Properties of 2D Ti3C2Tx MXene Monolayers and Bilayers," Sci. Adv., **4 (6)**(June), pp. 1–7.

[161] Zhang, J., Kong, N., Uzun, S., Levitt, A., Seyedin, S., Lynch, P. A., Qin, S., Han, M., Yang, W., Liu, J., Wang, X., Gogotsi, Y., and Razal, J. M., 2020, "MXene Films Scalable Manufacturing of Free-Standing, Strong Ti3C2Tx MXene Films with Outstanding Conductivity," Adv. Mater., **32**(23).

[162] Lukatskaya, M. R., Kota, S., Lin, Z., Zhao, M. Q., Shpigel, N., Levi, M. D., Halim, J., Taberna, P. L., Barsoum, M. W., Simon, P., and Gogotsi, Y., 2017, "Ultra-High-Rate Pseudocapacitive Energy Storage in Two-Dimensional Transition Metal Carbides," Nat. Energy, **6**.

[163] Aslam, M. K., Niu, Y., and Xu, M., 2021, "MXenes for Non-Lithium-Ion (Na, K, Ca, Mg, and Al) Batteries and Supercapacitors," Adv. Energy Mater., **11**(2).

[164] Ming, F., Liang, H., Huang, G., Bayhan, Z., and Alshareef, H. N., 2021, "MXenes for Rechargeable Batteries Beyond the Lithium-Ion," Adv. Mater., **33**(1).

[165] Liang, X., Garsuch, A., and Nazar, L. F., 2015, "Sulfur Cathodes Based on Conductive MXene Nanosheets for High-Performance Lithium-Sulfur Batteries," Angew. Chemie - Int. Ed., **54**(13), pp. 3907–3911.

[166] Gao, X.-T., Xie, Y., Zhu, X.-D., Sun, K.-N., Xie, X.-M., Liu, Y.-T., Yu, J.-Y., and Ding, B., 2018, "Li-S Batteries: Ultrathin MXene Nanosheets Decorated with TiO 2 Quantum Dots as an Efficient Sulfur Host toward Fast and Stable Li-S Batteries," Small, **14**(41), p. 1870190.

[167] Xiao, Z., Li, Z., Meng, X., and Wang, R., 2019, "MXene-Engineered Lithium-Sulfur Batteries," J. Mater. Chem. A, **7**(40), pp. 22730–22743.

[168] Zhao, Q., Zhu, Q., Liu, Y., and Xu, B., 2021, "Status and Prospects of MXene-Based Lithium–Sulfur Batteries," Adv. Funct. Mater., **31**(21).

[169] Naguib, M., Come, J., Dyatkin, B., Presser, V., Taberna, P. L., Simon, P., Barsoum, M. W., and Gogotsi, Y., 2012, "MXene: A Promising Transition Metal Carbide Anode for Lithium-Ion Batteries," Electrochem. commun., **16**(1), pp. 61–64.

[170] Thapaliya, B. P., Jafta, C. J., Lyu, H., Xia, J., Meyer, H. M., Paranthaman, M. P., Sun, X. G., Bridges, C. A., and Dai, S., 2019, "Fluorination of MXene by Elemental F2 as Electrode Material for Lithium-Ion Batteries," ChemSusChem, **12**(7), pp. 1316–1324.

[171] Huang, Y., Yang, H., Zhang, Y., Zhang, Y., Wu, Y., Tian, M., Chen, P., Trout, R., Ma, Y., Wu, T. H., Wu, Y., and Liu, N., 2019, "A Safe and Fast-Charging Lithium-Ion Battery Anode Using MXene Supported Li3VO4," J. Mater. Chem. A, **7**(18), pp. 11250–11256.

[172] Liu, R., Cao, W., Han, D., Mo, Y., Zeng, H., Yang, H., and Li, W., 2019, "Nitrogen-

Doped Nb2CTx MXene as Anode Materials for Lithium Ion Batteries," J. Alloys Compd., **793**, pp. 505–511.

[173] Cai, L., Li, Z., Zhang, S., Prenger, K., Naguib, M., and Pol, V. G., 2021, "Safer Lithium-Ion Battery Anode Based on Ti3C2Tz MXene with Thermal Safety Mechanistic Elucidation," Chem. Eng. J., **419**(February), p. 129387.

[174] Tang, Q., Zhou, Z., and Shen, P., 2012, "Are MXenes Promising Anode Materials for Li Ion Batteries? Computational Studies on Electronic Properties and Li Storage Capability of Ti3C2 and Ti3C2X2 (X = F, OH) Monolayer," J. Am. Chem. Soc., **134**(40), pp. 16909–16916.

[175] Iqbal, A., Sambyal, P., and Koo, C. M., 2020, "Electromagnetic Interference Shielding: 2D MXenes for Electromagnetic Shielding: A Review," Adv. Funct. Mater., **30**(47), p. 2070307.

[176] Wang, J. F., Kang, H., Cheng, Z. J., Xie, Z. M., Wang, Y. S., Liu, Y. Y., and Fan, Z. M., 2021, "Research Progress in Ti3C2Tx MXene- Based Electromagnetic Interference Shielding Material," Cailiao Gongcheng/Journal Mater. Eng., **49**(6), pp. 14–25.

[177] Ji, B., Fan, S., Ma, X., Hu, K., Wang, L., Luan, C., Deng, J., Cheng, L., and Zhang, L., 2020, "Electromagnetic Shielding Behavior of Heat-Treated Ti3C2TX MXene Accompanied by Structural and Phase Changes," Carbon N. Y., **165**, pp. 150–162.

[178] Han, M., Liu, Y., Rakhmanov, R., Israel, C., Tajin, M. A. S., Friedman, G., Volman, V., Hoorfar, A., Dandekar, K. R., and Gogotsi, Y., 2021, "Solution-Processed Ti3C2Tx MXene Antennas for Radio-Frequency Communication," Adv. Mater., **33**(1).

[179] Al-Hamadani, Y. A. J., Jun, B. M., Yoon, M., Taheri-Qazvini, N., Snyder, S. A., Jang, M., Heo, J., and Yoon, Y., 2020, "Applications of MXene-Based Membranes in Water Purification: A Review," Chemosphere, **254**, p. 126821.

[180] Ihsanullah, I., 2020, "MXenes (Two-Dimensional Metal Carbides) as Emerging Nanomaterials for Water Purification: Progress, Challenges and Prospects," Chem. Eng. J., **388**(December 2019), p. 124340.

[181] Guo, Y., Zhong, M., Fang, Z., Wan, P., and Yu, G., 2019, "A Wearable Transient Pressure Sensor Made with MXene Nanosheets for Sensitive Broad-Range Human-Machine Interfacing," Nano Lett., **19**(2), pp. 1143–1150.

[182] Kalambate, P. K., Gadhari, N. S., Li, X., Rao, Z., Navale, S. T., Shen, Y., Patil, V. R., and Huang, Y., 2019, "Recent Advances in MXene–Based Electrochemical Sensors and Biosensors," TrAC - Trends Anal. Chem., **120**, p. 115643.

[183] Lin, H., Chen, Y., and Shi, J., 2018, "Insights into 2D MXenes for Versatile Biomedical Applications: Current Advances and Challenges Ahead," Adv. Sci., **5**(10).

[184] Hu, J., Li, S., Zhang, J., Chang, Q., Yu, W., and Zhou, Y., 2020, "Mechanical Properties and Frictional Resistance of Al Composites Reinforced with Ti3C2Tx MXene," Chinese Chem. Lett., **31**(4), pp. 996–999.

[185] Li, M., Wang, S., Wang, Q., Ren, F., and Wang, Y., 2021, "Microstructure and Tensile Properties of Ni Nano Particles Modified MXene Reinforced Copper Matrix Composites," Mater. Sci. Eng. A, **808**(February), p. 140932.

[186] Wyatt, B. C., Nemani, S. K., and Anasori, B., 2021, "2D Transition Metal Carbides (MXenes) in Metal and Ceramic Matrix Composites," Nano Converg., **8**(1).

[187] Fei, M., Lin, R., Lu, Y., Zhang, X., Bian, R., Cheng, J., Luo, P., Xu, C., and Cai, D., 2017, "MXene-Reinforced Alumina Ceramic Composites," Ceram. Int., **43**(18), pp. 17206–17210.

[188] Guo, J., Legum, B., Anasori, B., Wang, K., Lelyukh, P., Gogotsi, Y., and Randall, C. A., 2018, "Cold Sintered Ceramic Nanocomposites of 2D MXene and Zinc Oxide," Adv. Mater., **30**(32).

[189] Sokol, M., Natu, V., Kota, S., and Barsoum, M. W., 2019, "On the Chemical Diversity of the MAX Phases," Trends Chem., **1**(2), pp. 210–223.

[190] Cheng, Y., Zhang, Y., Li, Y., Dai, J., and Song, Y., 2019, "Hierarchical Ni2P/Cr2CTx (MXene) Composites with Oxidized Surface Groups as Efficient Bifunctional Electrocatalysts for Overall Water Splitting," J. Mater. Chem. A, **7**(15), pp. 9324–9334.

[191] Sun, Q., Fu, Z., and Yang, Z., 2020, "Tunable Magnetic and Electronic Properties of the Cr-Based MXene (Cr2C) with Functional Groups and Doping," J. Magn. Magn. Mater., **514**(June).

[192] Hart, J. L., Hantanasirisakul, K., Lang, A. C., Anasori, B., Pinto, D., Pivak, Y., van Omme, J. T., May, S. J., Gogotsi, Y., and Taheri, M. L., 2019, "Control of MXenes' Electronic Properties through Termination and Intercalation," Nat. Commun., **10**(1).

[193] Anasori, B., Shi, C., Moon, E. J., Xie, Y., Voigt, C. A., Kent, P. R. C., May, S. J., Billinge, S. J. L., Barsoum, M. W., and Gogotsi, Y., 2016, "Control of Electronic Properties of 2D Carbides (MXenes) by Manipulating Their Transition Metal Layers," Nanoscale Horizons, **1**(3), pp. 227–234.

[194] Seredych, M., Shuck, C. E., Pinto, D., Alhabeb, M., Precetti, E., Deysher, G., Anasori, B., Kurra, N., and Gogotsi, Y., 2019, "High-Temperature Behavior and Surface Chemistry of Carbide MXenes Studied by Thermal Analysis," Chem. Mater., **31**(9), pp. 3324–3332.

[195] Ling, Z., Ren, C. E., Zhao, M., Yang, J., Giammarco, J. M., and Qiu, J., 2014, "Flexible and Conductive MXene Films and Nanocomposites with High Capacitance," Proc. Natl. Acad. Sci. U. S. A., **111**(47), pp. 1–6.

[196] Maleski, K., Mochalin, V. N., and Gogotsi, Y., 2017, "Dispersions of Two-Dimensional Titanium Carbide MXene in Organic Solvents," Chem. Mater., **29**(4), pp. 1632–1640.

[197] Wang, H., Wu, Y., Zhang, J., Li, G., Huang, H., Zhang, X., and Jiang, Q., 2015, "Enhancement of the Electrical Properties of MXene Ti3C2 Nanosheets by Post-Treatments of Alkalization and Calcination," Mater. Lett., **160**, pp. 537–540.

[198] Li, J., Du, Y., Huo, C., Wang, S., and Cui, C., 2015, "Thermal Stability of Two-Dimensional Ti2C Nanosheets," Ceram. Int., **41**(2), pp. 2631–2635.

[199] Li, J., Yuan, X., Lin, C., Yang, Y., Xu, L., Du, X., Xie, J., Lin, J., and Sun, J., 2017, "Achieving High Pseudocapacitance of 2D Titanium Carbide (MXene) by Cation Intercalation and Surface Modification," Adv. Energy Mater., **7**(15).

[200] Wang, K., Zhou, Y., Xu, W., Huang, D., Wang, Z., and Hong, M., 2016, "Fabrication and Thermal Stability of Two-Dimensional Carbide Ti3C2 Nanosheets," Ceram. Int., **42**(7), pp. 8419–8424.

[201] Persson, I., Näslund, L. Å., Halim, J., Barsoum, M. W., Darakchieva, V., Palisaitis, J., Rosen, J., and Persson, P. O. Å., 2018, "On the Organization and Thermal Behavior of Functional Groups on Ti3C2 MXene Surfaces in Vacuum," 2D Mater., **5**(1).

[202] Zhang, C. J., Pinilla, S., McEvoy, N., Cullen, C. P., Anasori, B., Long, E., Park, S. H., Seral-Ascaso, A., Shmeliov, A., Krishnan, D., Morant, C., Liu, X., Duesberg, G. S., Gogotsi, Y., and Nicolosi, V., 2017, "Oxidation Stability of Colloidal Two-Dimensional Titanium Carbides (MXenes)," Chem. Mater., **29**(11), pp. 4848–4856.

[203] Lotfi, R., Naguib, M., Yilmaz, D. E., Nanda, J., and Van Duin, A. C. T., 2018, "A Comparative Study on the Oxidation of Two-Dimensional Ti3C2 MXene Structures in Different Environments," J. Mater. Chem. A, **6**(26), pp. 12733–12743.

[204] Huang, S., and Mochalin, V. N., 2019, "Hydrolysis of 2D Transition-Metal Carbides (MXenes) in Colloidal Solutions," Inorg. Chem., **58**(3), pp. 1958–1966.

[205] Xia, F., Lao, J., Yu, R., Sang, X., Luo, J., Li, Y., and Wu, J., 2019, "Ambient Oxidation of Ti3C2 MXene Initialized by Atomic Defects," Nanoscale, **11**(48), pp. 23330–23337.

[206] Lee, Y., Kim, S. J., Kim, Y. J., Lim, Y., Chae, Y., Lee, B. J., Kim, Y. T., Han, H., Gogotsi, Y., and Ahn, C. W., 2020, "Oxidation-Resistant Titanium Carbide MXene Films," J. Mater. Chem. A, **8**(2), pp. 573–581.

[207] Hemmat, Z., Yasaei, P., Schultz, J. F., Hong, L., Majidi, L., Behranginia, A., Verger, L., Jiang, N., Barsoum, M. W., Klie, R. F., and Salehi-Khojin, A., 2019, "Tuning Thermal Transport Through Atomically Thin Ti3C2Tz MXene by Current Annealing in Vacuum," Adv. Funct. Mater., **29**(19).

[208] Fredrickson, K. D., Anasori, B., Seh, Z. W., Gogotsi, Y., and Vojvodic, A., 2016, "Effects of Applied Potential and Water Intercalation on the Surface Chemistry of Ti2C and Mo2C MXenes," J. Phys. Chem. C, **120**(50), pp. 28432–28440.

[209] Lu, M., Li, H., Han, W., Chen, J., Shi, W., Wang, J., Meng, X. M., Qi, J., Li, H., Zhang, B., Zhang, W., and Zheng, W., 2019, "2D Titanium Carbide (MXene) Electrodes with Lower-F Surface for High Performance Lithium-Ion Batteries," J. Energy Chem., **31**, pp. 148–153.

[210] Rasel, M. A. J., Wyatt, B., Wetherington, M., Anasori, B., and Haque, A., 2021, "Low-Temperature Annealing of 2D Ti3C2Tx MXene Films Using Electron Wind Force in

Ambient Conditions," J. Mater. Res., **36**(17), pp. 3398–3406.

[211] Schetky, L. M., 2007, "Shape-Memory Alloys as Multifunctional Materials," *Intelligent Materials*, M. Shahinpoor, and H.-J. Schneider, eds., pp. 317–338.

[212] Duerig, T., Pelton, A., and Sto, D., 1999, "An Overview of Nitinol Medical Applications," Mater. Sci. Eng. A, **273**–**275**, pp. 149–160.

[213] Zhu, R. F., Liu, J. N., Tang, G. Y., Shi, S. Q., Fu, M. W., and Tse, Z. T. H., 2014, "The Improved Superelasticity of NiTi Alloy via Electropulsing Treatment for Minutes," J. Alloys Compd., **584**, pp. 225–231.

[214] Otsuka, K., and Ren, X., 2005, "Physical Metallurgy of Ti-Ni-Based Shape Memory Alloys," Prog. Mater. Sci., **50**(5), pp. 511–678.

[215] Prokoshkin, S. D., Khmelevskaya, I. Y., Dobatkin, S. V., Trubitsyna, I. B., Tatyanin, E. V., Stolyarov, V. V., and Prokofiev, E. A., 2005, "Alloy Composition, Deformation Temperature, Pressure and Post-Deformation Annealing Effects in Severely Deformed Ti-Ni Based Shape Memory Alloys," Acta Mater., **53**(9), pp. 2703–2714.

[216] Mantovani, D., 2000, "Shape Memory Alloys: Properties and Biomedical Applications," Jom, **52**(10), pp. 36–44.

[217] Otsuka, K., and Ren, X., 1999, "Recent Developments in the Research of Shape Memory Alloys," Intermetallics, **7**(5), pp. 511–528.

[218] Johnson, A. D., 1991, "Vacuum-Deposited Tini Shape Memory Film: Characterization and Applications in Microdevices," J. Micromechanics Microengineering, **1**(1), pp. 34–41.

[219] Miyazaki, S., and Ishida, A., 1994, "Shape Memory Characteristics of Sputter-Deposited Ti-Ni Thin Films," Mater. Trans. JIM, **35**(1), pp. 14–19.

[220] Miyazaki, S., and Ishida, A., 1999, "Martensitic Transformation and Shape Memory Behavior in Sputter-Deposited TiNi-Base Thin Films," Mater. Sci. Eng. A, **273**–**275**, pp. 106–133.

[221] Ishida, A., Sato, M., Kimura, T., and Miyazaki, S., 2000, "Stress-Strain Curves of Sputter-Deposited Ti-Ni Thin Films," Philos. Mag. A Phys. Condens. Matter, Struct. Defects Mech. Prop., **80**(4), pp. 967–980.

[222] Malard, B., Pilch, J., Sittner, P., Delville, R., and Curfs, C., 2011, "In Situ Investigation of the Fast Microstructure Evolution during Electropulse Treatment of Cold Drawn NiTi Wires," Acta Mater., **59**(4), pp. 1542–1556.

[223] Zhang, Y., Jiang, S., Hu, L., and Liang, Y., 2013, "Deformation Mechanism of NiTi Shape Memory Alloy Subjected to Severe Plastic Deformation at Low Temperature," Mater. Sci. Eng. A, **559**, pp. 607–614.

[224] Wu, S. K., Lin, H. C., and Yeh, C. H., 2000, "A Comparison of the Cavitation Erosion Resistance of TiNi Alloys, SUS304 Stainless Steel and Ni-Based Self-Fluxing Alloy,"

Wear, **244**(1–2), pp. 85–93.

[225] Fadlallah, S. A., El-Bagoury, N., Gad El-Rab, S. M. F., Ahmed, R. A., and El-Ousamii, G., 2014, "An Overview of NiTi Shape Memory Alloy: Corrosion Resistance and Antibacterial Inhibition for Dental Application," J. Alloys Compd., **583**, pp. 455–464.

[226] Köhl, M., Bram, M., Moser, A., Buchkremer, H. P., Beck, T., and Stöver, D., 2011, "Characterization of Porous, Net-Shaped NiTi Alloy Regarding Its Damping and Energy-Absorbing Capacity," Mater. Sci. Eng. A, **528**(6), pp. 2454–2462.

[227] Morgan, N. B., 2004, "Medical Shape Memory Alloy Applications - The Market and Its Products," Mater. Sci. Eng. A, **378**(1-2 SPEC. ISS.), pp. 16–23.

[228] Elahinia, M. H., Hashemi, M., Tabesh, M., and Bhaduri, S. B., 2012, "Manufacturing and Processing of NiTi Implants: A Review," Prog. Mater. Sci., **57**(5), pp. 911–946.

[229] Gu, Y. W., Tay, B. Y., Lim, C. S., and Yong, M. S., 2005, "Biomimetic Deposition of Apatite Coating on Surface-Modified NiTi Alloy," Biomaterials, **26**(34), pp. 6916–6923.

[230] Schiff, N., Grosgogeat, B., Lissac, M., and Dalard, F., 2002, "Influence of Fluoride Content and PH on the Corrosion Resistance of Titanium and Its Alloys," Biomaterials, **23**(9), pp. 1995–2002.

[231] Torrisi, L., 1999, "The NiTi Superelastic Alloy Application to the Dentistry Field," Biomed. Mater. Eng., **9**(1), pp. 39–47.

[232] Humbeeck, J. Van, 1999, "Non-Medical Applications of Shape Memory Alloys," Mater. Sci. Eng. A, **273**–**275**, pp. 134–148.

[233] Ren, X., and Otsuka, K., 2000, "Why Does the Martensitic Transformation Temperature Strongly Depend on Composition?," Mater. Sci. Forum, **327**–**328**, pp. 429–432.

[234] Stroz, D., Kwarciak, J., and Morawiec, H., 1988, "Effect of Ageing on Martensitic Transformation in NiTi Shape Memory Alloy," J. Mater. Sci., **23**(11), pp. 4127–4131.

[235] Jiang, F., Li, L., Zheng, Y., Yang, H., and Liu, Y., 2008, "Cyclic Ageing of Ti-50.8 at.% Ni Alloy," Intermetallics, **16**(3), pp. 394–398.

[236] Pelton, A. R., DiCello, J., and Miyazaki, S., 2000, "Optimisation of Processing and Properties of Medical Grade Nitinol Wire," Minim. Invasive Ther. Allied Technol., **9**(2), pp. 107–118.

[237] Liu, X., Wang, Y., Yang, D., and Qi, M., 2008, "The Effect of Ageing Treatment on Shape-Setting and Superelasticity of a Nitinol Stent," Mater. Charact., **59**(4), pp. 402–406.

[238] Undisz, A., Fink, M., and Rettenmayr, M., 2008, "Response of Austenite Finish Temperature and Phase Transformation Characteristics of Thin Medical-Grade Ni-Ti Wire to Short-Time Annealing," Scr. Mater., **59**(9), pp. 979–982.

[239] Morgan, N. B., and Broadley, M., 2004, "Taking the Art Out of Smart!-Forming Processes

and Durability Issues for the Application of NiTi Shape Memory Alloys in Medical Devices," *Medical Device Materials: Proceedings from the Materials & Processes for Medical Devices Conference*, ASM International, Materials Park, OH, pp. 247–252.

[240] Tsuchiya, K., Hada, Y., Koyano, T., Nakajima, K., Ohnuma, M., Koike, T., Todaka, Y., and Umemoto, M., 2009, "Production of TiNi Amorphous/Nanocrystalline Wires with High Strength and Elastic Modulus by Severe Cold Drawing," Scr. Mater., **60**(9), pp. 749–752.

[241] Li, Z., Cheng, X., and Shangguan, Q., 2005, "Effects of Heat Treatment and ECAE Process on Transformation Behaviors of TiNi Shape Memory Alloy," Mater. Lett., **59**(6), pp. 705–709.

[242] Schaffer, J. E., 2009, "Structure-Property Relationships in Conventional and Nanocrystalline NiTi Intermetallic Alloy Wire," J. Mater. Eng. Perform., **18**(5–6), pp. 582–587.

[243] Malard, B., Pilch, J., Sittner, P., Gartnerova, V., Delville, R., Schryvers, D., and Curfs, C., 2009, "Microstructure and Functional Property Changes in Thin NiTi Wires Heat Treated by Electric Current - High Energy X-Ray and Tem Investigations," Funct. Mater. Lett., **2**(2), pp. 45–54.

[244] Adharapurapu, R. R., Jiang, F., and Vecchio, K. S., 2010, "Aging Effects on Hardness and Dynamic Compressive Behavior of Ti-55Ni (at.%) Alloy," Mater. Sci. Eng. A, **527**(7–8), pp. 1665–1676.

[245] Khalil-Allafi, J., Dlouhy, A., and Eggeler, G., 2002, "Ni4Ti3-Precipitation during Aging of NiTi Shape Memory Alloys and Its Influence on Martensitic Phase Transformations," Acta Mater., **50**(17), pp. 4255–4274.

[246] Zheng, Y., Jiang, F., Li, L., Yang, H., and Liu, Y., 2008, "Effect of Ageing Treatment on the Transformation Behaviour of Ti-50.9 at.% Ni Alloy," Acta Mater., **56**(4), pp. 736–745.

[247] Cao, S., Nishida, M., and Schryvers, D., 2011, "Quantitative Three-Dimensional Analysis of Ni4Ti3 Precipitate Morphology and Distribution in Polycrystalline Ni-Ti," Acta Mater., **59**(4), pp. 1780–1789.

[248] Wang, Z. G., Zu, X. T., Feng, X. D., Zhu, S., Deng, J., and Wang, L. M., 2004, "Effect of Electrothermal Annealing on the Transformation Behavior of TiNi Shape Memory Alloy and Two-Way Shape Memory Spring Actuated by Direct Electrical Current," Phys. B Condens. Matter, **349**(1–4), pp. 365–370.

[249] Wang, Y. B., Zheng, Y. F., and Liu, Y., 2009, "Effect of Short-Time Direct Current Heating on Phase Transformation and Superelasticity of Ti-50.8at.%Ni Alloy," J. Alloys Compd., **477**(1–2), pp. 764–767.

[250] Miller, D. A., and Lagoudas, D. C., 2001, "Influence of Cold Work and Heat Treatment on the Shape Memory Effect and Plastic Development of NiTi," Mater. Sci. Eng. A, **308**(1–2), pp. 161–175.

[251] Liu, Y., Yang, H., and Voigt, A., 2003, “Thermal Analysis of the Effect of Aging on the Transformation Behaviour of Ti-50.9at.% Ni,” Mater. Sci. Eng. A, **360**(1–2), pp. 350–355.

[252] Tan, G., and Liu, Y., 2004, “Comparative Study of Deformation-Induced Martensite Stabilisation via Martensite Reorientation and Stress-Induced Martensitic Transformation in NiTi,” Intermetallics, **12**(4), pp. 373–381.

[253] Stolyarov, V. V., Ugurchiev, U. K., Gurtovaya, I. B., and Prokoshkin, S. D., 2008, “Increase in the Deformability of Coarse-Grained TiNi Alloy Rolled with Superimposition of Pulse Current,” Met. Sci. Heat Treat., **50**(3–4), pp. 132–135.

[254] Prokoshkin, S. D., Stolyarov, V. V., Korotitskii, A. V., Inaekyan, K. E., Danilov, E. S., Khmelevskaya, I. Y., Glezer, A. M., Makushev, S. Y., and Ugurchiev, U. K., 2009, “Investigation of the Influence of the Parameters of Pulsed Electric Action upon Deformation on the Structure and Functional Properties of a Ti-Ni Alloy with a Shape-Memory Effect,” Phys. Met. Metallogr., **108**(6), pp. 616–624.

[255] Delville, R., Malard, B., Pilch, J., Sittner, P., and Schryvers, D., 2010, “Microstructure Changes during Non-Conventional Heat Treatment of Thin Ni-Ti Wires by Pulsed Electric Current Studied by Transmission Electron Microscopy,” Acta Mater., **58**(13), pp. 4503–4515.

[256] Zhu, R. F., Tang, G. Y., Shi, S. Q., Fu, M. W., and Gromov, V. E., 2013, “Effect of Electropulsing Treatment on the Microstructure and Superelasticity of TiNi Alloy,” Appl. Phys. A Mater. Sci. Process., **111**(4), pp. 1195–1201.

[257] Cao, W. H., Zhang, J. L., and Shek, C. H., 2013, “Effects of Electropulsing Treatment on Mechanical Properties in Ti Rich TiNi Shape Memory Alloy,” Mater. Sci. Technol. (United Kingdom), **29**(9), pp. 1135–1138.

[258] Zhu, R., Jiang, Y., Guan, L., Li, H., and Tang, G., 2016, “Difference in Recrystallization between Electropulsing-Treated and Furnace-Treated NiTi Alloy,” J. Alloys Compd., **658**, pp. 548–554.

[259] Zhu, R., and Tang, G., 2017, “The Improved Plasticity of NiTi Alloy via Electropulsing in Rolling,” Mater. Sci. Technol. (United Kingdom), **33**(5), pp. 546–551.

[260] Sarycheva, A., and Gogotsi, Y., 2020, “Raman Spectroscopy Analysis of the Structure and Surface Chemistry of Ti3C2T XMXene,” Chem. Mater., **32**(8), pp. 3480–3488.

[261] Lioi, D. B., Neher, G., Heckler, J. E., Back, T., Mehmood, F., Nepal, D., Pachter, R., Vaia, R., and Kennedy, W. J., 2019, “Electron-Withdrawing Effect of Native Terminal Groups on the Lattice Structure of Ti3C2Tx MXenes Studied by Resonance Raman Scattering: Implications for Embedding MXenes in Electronic Composites,” ACS Appl. Nano Mater., **2**(10), pp. 6087–6091.

[262] Hu, T., Wang, J., Zhang, H., Li, Z., Hu, M., and Wang, X., 2015, “Vibrational Properties of Ti3C2 and Ti3C2T2 (T = O, F, OH) Monosheets by First-Principles Calculations: A Comparative Study,” Phys. Chem. Chem. Phys., **17**(15), pp. 9997–10003.